Monthly Notices
of the
ROYAL ASTRONOMICAL SOCIETY

MNRAS **458,** 3851–3866 (2016)
Advance Access publication 2016 March 7

doi:10.1093/mnras/stw541

Mid-infrared imaging- and spectro-polarimetric subarcsecond observations of NGC 1068

E. Lopez-Rodriguez,[1,2]★ C. Packham,[3,4] P. F. Roche,[5] A. Alonso-Herrero,[3,5,6] T. Díaz-Santos,[7,8] R. Nikutta,[9] O. González-Martín,[10] C. A. Álvarez,[11,12] P. Esquej,[13] J. M. Rodríguez Espinosa,[11,12] E. Perlman,[14] C. Ramos Almeida[11,12] and C. M. Telesco[15]

[1]*Department of Astronomy, University of Texas at Austin, 1 University Station C1400, Austin, TX 78712, USA*
[2]*McDonald Observatory, University of Texas at Austin, Austin, TX 78712, USA*
[3]*Department of Physics and Astronomy, University of Texas at San Antonio, One UTSA Circle, San Antonio, TX 78249, USA*
[4]*National Astronomical Observatory of Japan, Mitaka, Tokyo 181-8588, Japan*
[5]*Astrophysics, Department of Physics, University of Oxford, DWB, Keble Road, Oxford OX1 3RH, UK*
[6]*Instituto de Física de Cantabria, CSIC-UC, E-39005 Santander, Spain*
[7]*Infrared Processing and Analysis Center, MS 100-22, California Institute of Technology, Pasadena, CA, USA*
[8]*Núcleo de Astronomía de la Facultad de Ingeniería, Universidad Diego Portales, Av. Ejercito Libertador 441, Santiago, Chile*
[9]*Instituto de Astrofísica, Facultad de Física, Pontificia Universidad Católica de Chile, 306, Santiago 22, Chile*
[10]*Centro de Radioastronomía y Astrofísica (CRyA-UNAM), 3-72 (Xangari), 8701 Morelia, Mexico*
[11]*Departamento de Astrofísica, Universidad de La Laguna (ULL), E-38206 La Laguna, Tenerife, Spain*
[12]*Instituto de Astrofísica de Canarias (IAC), E-38205 La Laguna, Tenerife, Spain*
[13]*Departamento de Astrofísica, Facultad de CC. Físicas, Universidad Complutense de Madrid, E-28040 Madrid, Spain*
[14]*Florida Institute of Technology, Melbourne, FL 32901, USA*
[15]*Department of Astronomy, University of Florida, 211 Bryant Space Science Center, PO Box 11205, Gainesville, FL 32611-2055, USA*

Accepted 2016 March 3. Received 2016 March 1; in original form 2015 August 4

ABSTRACT

We present subarcsecond 7.5–13 μm imaging- and spectro-polarimetric observations of NGC 1068 using CanariCam on the 10.4-m Gran Telescopio CANARIAS. At all wavelengths, we find: (1) A 90 × 60 pc extended polarized feature in the northern ionization cone, with a uniform ∼44° polarization angle. Its polarization arises from dust and gas emission in the ionization cone, heated by the active nucleus and jet, and further extinguished by aligned dust grains in the host galaxy. The polarization spectrum of the jet–molecular cloud interaction at ∼24 pc from the core is highly polarized, and does not show a silicate feature, suggesting that the dust grains are different from those in the interstellar medium. (2) A southern polarized feature at ∼9.6 pc from the core. Its polarization arises from a dust emission component extinguished by a large concentration of dust in the galaxy disc. We cannot distinguish between dust emission from magnetically aligned dust grains directly heated by the jet close to the core, and aligned dust grains in the dusty obscuring material surrounding the central engine. Silicate-like grains reproduce the polarized dust emission in this feature, suggesting different dust compositions in both ionization cones. (3) An upper limit of polarization degree of 0.3 per cent in the core. Based on our polarization model, the expected polarization of the obscuring dusty material is $\lesssim$0.1 per cent in the 8–13 μm wavelength range. This low polarization may be arising from the passage of radiation through aligned dust grains in the shielded edges of the clumps.

Key words: methods: observational – techniques: high angular resolution – techniques: polarimetric – galaxies: individual: NGC 1068 – galaxies: Seyfert – infrared: galaxies.

1 INTRODUCTION

NGC 1068 is the archetypal type 2 active galactic nucleus (AGN), whose proximity (D = 12.5 Mpc, and 1 arcsec = 60 pc, adopting H_0 = 73 km s^{-1} Mpc^{-1}) and high brightness make it an ideal target for polarimetry. This object is probably the best-studied AGN

★ E-mail: enrique.lopezrodriguez@utexas.edu

regarding polarimetry, and this has allowed us to obtain a better understanding of the AGN structure. The most important polarimetric study of NGC 1068, for the sake of the entire field, was certainly the detection of polarized broad emission lines in the optical (0.35–0.70 μm) wavelengths by Antonucci & Miller (1985). This detection is interpreted through scattering of the radiation from the central engine (black hole and accretion disc) into our line of sight (LOS) by matter in the ionization cones. This result allowed us to understand that the central engine of NGC 1068 is obscured by a dusty structure, giving a major boost to the unified model of AGN. The unified model (i.e. Lawrence 1991; Antonucci 1993; Urry & Padovani 1995) of AGN posits that the observational differences between AGN arise from the different orientations they present us. In this scheme, the AGN classification solely depends on the anisotropic obscuration of the central engine by the optically and geometrically thick distribution of dust.

Pioneering infrared (IR) polarimetric observations (Knacke & Capps 1974; Lebofsky, Kemp & Rieke 1978) found that the nucleus of NGC 1068 was highly obscured and polarized. The observed degree of polarization rises from 1.6 ± 0.4 per cent at 1.25 μm to 2.7 ± 0.2 per cent at 3.45 μm, and the position angle (PA) of polarization rotates from $99^\circ \pm 7^\circ$ at 1.25 μm to $125^\circ \pm 2^\circ$ at 3.45 μm in a 6 arcsec (360 pc) diameter aperture. They suggested that the IR polarization arises from an obscured power-law source, which is not directly observable at wavelengths shorter than 1 μm. Using 8–13 μm observations at the 3.9-m Anglo-Australian Telescope (AAT), Aitken et al. (1984) found a polarization spectrum with a uniform degree, 1.39 ± 0.09 per cent, and a PA of $54\overset{\circ}{.}8 \pm 1\overset{\circ}{.}9$ within apertures of 4.2 arcsec (252 pc) and 5.2 arcsec (312 pc) diameter. Although they were not able to rule out non-thermal processes, they suggested that dust emission from non-silicate and featureless grains is responsible for the mid-IR (MIR) polarization. Using these data and additional 0.36–4.8 μm broad-band imaging polarimetric observations, Bailey et al. (1988) concluded that the most likely polarization mechanism at near-IR (NIR) arises from the passage of centrally produced radiation through aligned dust grains in the obscuring dusty structure; a mechanism known as dichroic absorption. This result was further supported by the flip in the PA of polarization of $\sim 70^\circ$ from NIR to MIR. They interpreted this result as the change from dichroic absorption to dichroic emission from aligned dust grains in the dusty structure obscuring the central engine. At shorter wavelengths, a wavelength-independent intrinsic (after correction for starlight dilution) polarization of ∼16 per cent with a constant PA of $\sim 97^\circ$ from the ultraviolet (UV; Antonucci, Hurt & Miller 1994) to optical wavelengths (Antonucci & Miller 1985) was found. The fact that the PA of polarization at UV and optical is different to that in the NIR, suggests that different mechanisms of polarization dominate in these wavelength regimes. Further modelling (Young et al. 1995; Watanabe et al. 2003) and observations (Capetti et al. 1995; Packham et al. 1997; Lumsden et al. 1999; Simpson et al. 2002; Lopez-Rodriguez et al. 2015) have shown that electron scattering is the dominant polarization mechanism from UV to optical, whilst dust distributed within the 2–3 arcsec (120–180 pc) central region accounts for the polarization features in the IR (Bailey et al. 1988). Specifically, dichroic absorption from aligned dust grains within the dusty circumnuclear obscurer in NGC 1068 is the dominant polarization mechanism in the 1–5 μm wavelength range. Based on these studies, and together with the lack of evidence of variations in the PA of polarization over a period of months or years, non-thermal polarization mechanisms (e.g. synchrotron emission from a jet) can be ruled out as a polarization mechanism in the core of NGC 1068.

At large scales, imaging polarimetric observations (Scarrott et al. 1991) at the *V* band using the 3.9-m AAT showed that the optical polarization follows the arm and interarm structures of the galaxy. The degree of polarization increases in the large-scale inner bar (32 arcsec, 1.92 kpc) at a PA of 48°, the so-called NIR bar (Scoville et al. 1988; Schinnerer et al. 2000; Emsellem et al. 2006). Further high-spatial resolution optical (0.5–0.6 μm) polarimetric observations (Capetti et al. 1995) using the *Hubble Space Telescope* (*HST*) showed a centrosymmetric polarization pattern along the ionization cones in the ∼10 arcsec (600 pc) central region. This polarization pattern is the signature of a central point source whose radiation is ultimately polarized through scattering by dust and/or electrons (and which can be polarized from multiple scattering into the funnel of the obscuring dusty structure and/or broad-line clouds). At UV and optical wavelengths, these studies showed that electron scattering is the dominant polarization mechanism in the ionization cones of NGC 1068, with the optical polarization in the off-nuclear regions following the magnetic field of the NIR bar.

Using high-spatial resolution imaging polarimetric observations at 9.7 μm on the 8.1-m Gemini telescope, Packham et al. (2007) found complex polarization structures within the 2× 2 arcsec (120 pc × 120 pc) central region of NGC 1068. Specifically, (1) polarization arising from aligned dust grains in the narrow-line emission regions north of the core, (2) dust being channelled towards the central engine south, east and west of the core, and (3) a nuclear low, <0.6 per cent, polarization interpreted as the polarization arising from the compact (≤22 pc) obscuring dusty structure. Although only one filter was used in this study, making it difficult to disentangle the several polarization mechanisms, it showed the potential of MIR polarimetric observations to study the structure within and around AGN.

In this paper, we examine the interaction of the AGN with the surrounding dusty structures within the central 2 arcsec (120 pc) region of NGC 1068. We also put constraints on the polarization of the obscuring dusty structure. We performed subarcsecond resolution 8–13 μm imaging- and spectro-polarimetric observations using CanariCam on the 10.4-m Gran Telescopio CANARIAS (GTC) at the Roque de los Muchachos Observatory. The paper is organized as follows: Section 2 describes the observations and data reduction, Section 3 presents our polarimetric results. Polarization models are developed in Section 4 to explain the several polarization features, and then analysed and discussed in Section 5. In Section 6 we present the conclusions.

2 OBSERVATIONS AND DATA REDUCTION

2.1 Imaging polarimetry

NGC 1068 was observed on 2012 December 29 and 30, using the imaging polarimetric mode (Packham, Hough & Telesco 2005) of CanariCam (Telesco et al. 2003) on the 10.4-m GTC in Spain. CanariCam uses a 320 × 240 pixel Si:As Raytheon array, with a pixel scale of 0.0798 arcsec pixel^{-1}. The imaging polarimetric mode uses a half-wave retarder (half-wave plate, HWP), a field mask and a Wollaston prism. The Wollaston prism and HWP are made with sulphur-free CdSe. The HWP is chromatic, resulting in a variable polarimetric efficiency across the 7.5–13 μm wavelength range that has been well determined (Packham, Mason & Boreman 2008). This mode is usable across the entire wavelength range. In standard polarimetric observations, the HWP is set in four PA in the following sequence: $0^\circ, 45^\circ, 22\overset{\circ}{.}5$ and $67\overset{\circ}{.}5$. The field mask consisted of a series of slots of 320 pixels × 25 pixels each, corresponding

Table 1. Summary of observations.

Date (yyyymmdd)	λ (μm)	On-source time[a] (s)	FWHM$^{b}_{PSF}$ (arcsec)
		Imaging polarimetry	
20121229	8.7	1456	0.38
	10.3	2040	–
	11.3	1020	0.39
	11.6	1020	–
20121230	11.3	1894	0.39
		Spectropolarimetry	
20130722	7.5–13	1894	0.35

Notes. [a]For the imaging polarimetric observations, the total on-source time was estimated accounting for the positive and negative images, produced by the chop-nod technique, on the array. [b]FWHM of the PSF.

to a field of view (FOV) of 25.6 arcsec × 2.0 arcsec, where a total of three slots can be used, providing a non-contiguous total FOV of 25.6 arcsec × 6.0 arcsec.

The Si2 ($\lambda_c = 8.7$ μm, $\Delta\lambda = 1.1$ μm, 50 per cent cut-on/off), Si4 ($\lambda_c = 10.3$ μm, $\Delta\lambda = 0.9$ μm, 50 per cent cut-on/off) and Si5 ($\lambda_c = 11.6$ μm, $\Delta\lambda = 0.9$ μm, 50 per cent cut-on/off) filters provide the largest wavelength coverage with the best combination of sensitivity and spatial resolution for the filter set of CanariCam in the 10 μm atmospheric window. We thus used this combination of filters. Additionally, to study possible star formation regions in and around the core of NGC 1068, we performed observations using the PAH2 ($\lambda_c = 11.3$ μm, $\Delta\lambda = 0.6$ μm, 50 per cent cut-on/off) filter. Observations were made using a standard chop-nod technique to remove time-variable sky background and telescope thermal emission, and to reduce the effect of $1/f$ noise from the array/electronics. In all observations, the chop-throw was 8 arcsec, the chop-angle was 0° E of N, and the chop-frequency was 1.93 Hz. The angle of the short axis of the array with respect to north on the sky (i.e. instrumental position angle, IPA) was 90° E of N, and the telescope was nodded every 52 s along the chopping direction. Thus, only one slot with an FOV of 25.6 arcsec × 2.0 arcsec was used in the observations, with the negative images (produced by the chop-nod technique) within the same slot. For each filter, two observational sets were observed, except for the PAH2 filter where three observational sets (one observational set the first night and two observational sets the second night) were observed. A summary of the observations is shown in Table 1. To improve the signal-to-noise ratio (S/N) of the observations, the negative images on the array were also used, providing the total useful on-source time shown in Table 1.

Data were reduced using custom IDL routines. The difference for each chopped pair was calculated and the nod frames, then differenced and combined to create a single image per HWP PA. During this process, all nods were examined for high or variable background that could indicate the presence of clouds or variable precipitable water vapour. Fortunately, no data needed to be removed for these reasons. As NGC 1068 was observed in different sets, each HWP PA frame was registered and shifted to a common position, then images with the same HWP PA were co-added. Next, the ordinary (o-ray) and extraordinary (e-ray) rays, produced by a Wollaston prism, were extracted and the Stokes parameters I, Q and U were estimated according to the ratio method (e.g. Tinbergen 2005). Then, the degree $P = \sqrt{Q^2 + U^2}/I$ and PA $= 0.5 \arctan(U/Q)$, of polarization were estimated.

The instrumental polarization was corrected based on data provided by the GTC website.[1] Specifically, the instrumental polarization is $P_{ins} = 0.6 \pm 0.2$ per cent in all filters with a dependence on the PA of polarization given by $PA_{ins} = -(RMA + Elev) - 29.^{\circ}6$, where RMA is the Nasmyth rotator mechanical angle; and Elev is the telescope elevation. The instrumental polarization was corrected as follows. The normalized Stokes parameters, $q_{ins} = Q_{ins}/I_{ins}$ and $u_{ins} = U_{ins}/I_{ins}$, of the instrumental polarization were estimated using the degree P_{ins} and position angle PA_{ins} of the instrumental polarization. Then, q_{ins} and u_{ins} were subtracted from the normalized Stokes parameters of NGC 1068. Finally, the polarization efficiency was corrected based on data provided by the GTC website.[2] Specifically, the polarization efficiency is 90.3, 99.5, 95.9 and 97.0 per cent at 8.7, 10.3, 11.6 and 11.3 μm PAH, respectively. The measurements of the degree of polarization were corrected for polarization bias using the approach by Wardle & Kronberg (1974).

The polarized young stellar object, AFGL 2403, was observed at 8.7 and 11.3 μm immediately before NGC 1068, with an on-source time of 73 s in both filters. In total flux, AFGL 2403 was used as point-spread function (PSF) calibrator. Table 1 shows the full width at half-maximum (FWHM) of AFGL 2403, where a Moffat function with two parameters, FWHM and β, best described the delivered PSF (e.g. Radomski et al. 2008). In polarimetry, AFGL 2403 allowed us to characterize the polarization observations because it is bright, 95.2 Jy, and polarized, 1.5 ± 0.6 and 1.2 ± 0.3 per cent at 8.7 and 11.3 μm, respectively. The degree of polarization of AFGL 2403 corrected for instrumental polarization and polarization efficiency at 8.7 μm, was estimated at 1.3 ± 0.2 per cent. Our measurement is in excellent agreement with the degree of polarization of 1.4 ± 0.8 per cent at 8.7 μm measured by Smith et al. (2000, fig. 2). The zero-angle of the PA of polarization was calculated as the difference of the PA of polarization from our measurement, $\theta = 100^{\circ} \pm 2^{\circ}$, and Smith et al. (2000), $\theta_s = 39^{\circ} \pm 4^{\circ}$, i.e. $\Delta\theta_{8.7\,\mu m} = -61^{\circ} \pm 5^{\circ}$ at 8.7 μm. At other wavelengths, the zero-angle was estimated using the wavelength dependence of the PA of polarization observed by Smith et al. (2000, fig. 2).

Dedicated flux-standard stars were not observed. Flux calibration was performed using the N-band spectra observed with Michelle on the 8.1-m Gemini North (Mason et al. 2006). Specifically, flux calibration was performed using the spectral points at 8.7, 10.3, 11.3 and 11.6 μm of the 0.4 arcsec wide slit oriented 20° E of N and centred at the peak of NGC 1068 (see Mason et al. 2006, fig. 2). The extracted fluxes were 7.5, 8.3, 11.0 and 11.9 Jy, respectively. Then, measured counts in a 0.4 × 0.4 arcsec simulated slit aperture from our images at each wavelength were equated to the flux densities from the MIR spectra by Mason et al. (2006). Finally, the factor Jy counts^{-1} was estimated and used in the measurements of the flux densities in the several apertures shown in Section 3.1.1. These observations can be found at GTC Public Archive.

2.2 Spectropolarimetry

NGC 1068 was observed on 2013 July 22, during commissioning of the spectropolarimetric mode (Packham et al. 2005) of CanariCam on the 10.4-m GTC. The spectropolarimetric mode uses an HWP, a field mask, a slit and a Wollaston prism. A 0.41 arcsec

[1] Information at http://www.gtc.iac.es/instruments/canaricam/canaricam.php#Instrumental_Polarization

[2] Information at: http://www.gtc.iac.es/instruments/canaricam/canaricam.php#Polarization_Measurement_Efficiency

(∼5 pixels) wide slit oriented at 0° E of N to cover the north–south polarized features of NGC 1068 was used. The low resolution *N*-band ($\lambda_c = 10.4$ μm, $\Delta\lambda = 5.2$ μm, 50 per cent cut-on/off) grating was used, resulting in a dispersion of 0.019 μm pixel^{-1} and $R = \lambda/\Delta\lambda \sim 175$.

Observations were made using a standard chop-nod technique as described in Section 2.1 with a chop-throw of 8 arcsec, chop-angle of 90° E of N and a chop frequency of 1.93 Hz. The IPA was 0° E of N, and the telescope was nodded every 45.5 s along the chopping direction. Thus, only one slot with an FOV of 25.6 arcsec × 2.0 arcsec was used in these observations. We took two spectropolarimetric observational sets with an on-source time of 947 s each (Table 1). Before these observations, we obtained acquisition *N*-band imaging polarimetric observations with an on-source time of 79 s. The slit was aligned to the peak of the total flux of NGC 1068 to better than 2 pixels (0.16 arcsec).

Data were reduced as described in Section 2.1. For each spectropolarimetric observational set of NGC 1068, the o- and e-rays were extracted in two different locations (Section 3.2) of the slit: (1) PSF-extraction of the *southern feature*, and (2) at 0.35 arcsec (4.4 pixels) north of the peak of the total flux density image using a fixed 0.4 arcsec (5 pixels) aperture. CanariCam shows a slight (∼1 pixel) curvature across the array in the spectral direction, which was measured using the observations of the polarized young stellar object, AFGL 2591. This curvature was taken into account during the extraction of the spectra. For each observational set, Stokes parameters, *I*, *Q* and *U*, were estimated according to the ratio method, and then co-added to obtain the final spectra. Finally, the degree and PA of polarization were estimated.

The instrumental polarization was corrected as described in Section 2.1. The polarization efficiency was corrected using observations of the unpolarized standard star, HD 186791, through a wire-grid in the optical path of CanariCam. These observations allow us to estimate the polarization efficiency spectra of the HWP across the 7.5–13 μm wavelength range. The polarization efficiency was corrected by multiplying the spectrum of the degree of polarization of NGC 1068 by the inverse of the polarization efficiency spectrum. Although the variation of the polarization efficiency was accounted for, a variable S/N of the Stokes parameters as a function of the wavelength still remains. We corrected this effect by binning the *Q* and *U* spectra across the wavelength axis in bins of 0.285 μm (15 pixels) to obtain higher S/N across the spectrum. The measurements of the degree of polarization were corrected for polarization bias using the approach by Wardle & Kronberg (1974).

The polarized young stellar object, AFGL 2591, was observed using the spectropolarimetric mode immediately before NGC 1068. In total flux, AFGL 2591 was used as a PSF calibrator, giving us the FWHM across the wavelength range for the PSF-extracted spectra. A Moffat function with two parameters, FWHM and β, best described the delivered PSF. In polarimetry, AFGL 2591 allowed us to estimate the zero-angle calibration of the observations because it is bright, 281.5 Jy, and highly polarized, 5.6 ± 1 per cent (Smith et al. 2000, fig. 2). The zero-angle calibration, $\Delta\theta$, was estimated as the difference of the measured PA of polarization of our observations, $\theta = 58.^{\circ}5 \pm 0.^{\circ}3$, and the PA of polarization by Smith et al. (2000), $\theta_s = 170^{\circ} \pm 1^{\circ}$. We measured a constant PA of polarization across the 7.5–13 μm wavelength range, in excellent agreement with Smith et al. (2000). Thus, the zero-angle of polarization was estimated to be $\Delta\theta = \theta_s - \theta = 111.^{\circ}5 \pm 1.^{\circ}0$.

The total flux spectrum of NGC 1068 was wavelength calibrated to an accuracy of 0.019 μm pixel^{-1} using 10 μm window sky lines present in the spectrum. Then, the total flux spectrum was binned to a spectral resolution of 0.076 μm (4 pixels) to improve the S/N. Next, the spectrum of NGC 1068 was divided by the spectrum of the standard star, HD 186791 (K3III). Cohen & Davies (1995) show that late K and M stars have fundamental vibration–vibration bands of SiO in their spectra, which significantly depress the spectrum in the 7.5–10 μm wavelength range, and therefore affect the ratio with the science object. To remove this band and obtain the original spectrum of NGC 1068, the total flux spectrum of NGC 1068 was multiplied by the template spectrum of the standard star HD 186791, provided by the Gemini website.[3] Flux calibration was achieved by using the *N*-band spectra of NGC 1068 (in Jy) observed with Michelle on the 8.1-m Gemini North (Mason et al. 2006). The measured nuclear spectrum (in counts) in a 0.4 arcsec aperture was extracted and equated to the flux density from the MIR spectrum by Mason et al. (2006). The factor Jy counts^{-1} was estimated and used in several extractions of the spectra from our observations.

3 RESULTS

3.1 Imaging polarimetry

3.1.1 Photometry

Fig. 1 shows the total flux images at 8.7, 10.3, 11.6, and 11.3 μm (PAH). At all wavelengths NGC 1068 appears as an unresolved core in the E–W direction, with extended emission along N–S. The N–S extended emission slightly bends to the N-W direction up to 0.5 arcsec (30 pc), and then to the N-E direction up to 1.4 arcsec (84 pc); this feature was termed as *'tongue'* (see Bock et al. 2000, fig. 2). At 1.4 arcsec N-E from the core, the *NE knot* is located. These structures are in excellent agreement with previously published high-spatial resolution MIR observations (e.g. Bock et al. 2000; Tomono et al. 2001; Galliano et al. 2005; Poncelet et al. 2007).

We made measurements of the nuclear total flux density images centred at the peak of the total flux density at several diameter apertures (hereafter, aperture refers to diameter) to compare with previously published values (Table 2). In all cases, photometric errors were estimated by the variation of the counts in subsets of the data. Our photometric measurements are consistent with published flux density measurements. We also made photometric measurements of the *southern feature* and *north knot* (Section 3.1.2, Figs 2 and 3) in a 0.4 arcsec (24 pc) aperture centred on the peaks of polarized flux, for all features, and at each wavelength (Figs 2 and 3).

3.1.2 Polarimetry

Fig. 2 shows the polarized flux images with the overlaid polarization vectors at 8.7, 10.3, 11.6 and 11.3 μm (PAH). In these figures, the overlaid polarization vectors are proportional in length to the degree of polarization, and their orientation shows the PA of polarization. Only polarization vectors with $P/\sigma_p \geq 3$ are shown. σ_p is the uncertainty of the degree of polarization per pixel, estimated as $\sigma_p = \sqrt{\sigma_q^2 + \sigma_u^2}$, where σ_q and σ_u are the uncertainties of the normalized Stokes parameters (Wardle & Kronberg 1974). Fig. 3 shows the contours of the degree and PA of polarization for those

[3] Template at http://www.gemini.edu/sciops/instruments/mid-ir-resources/spectroscopic-calibrations#waveca

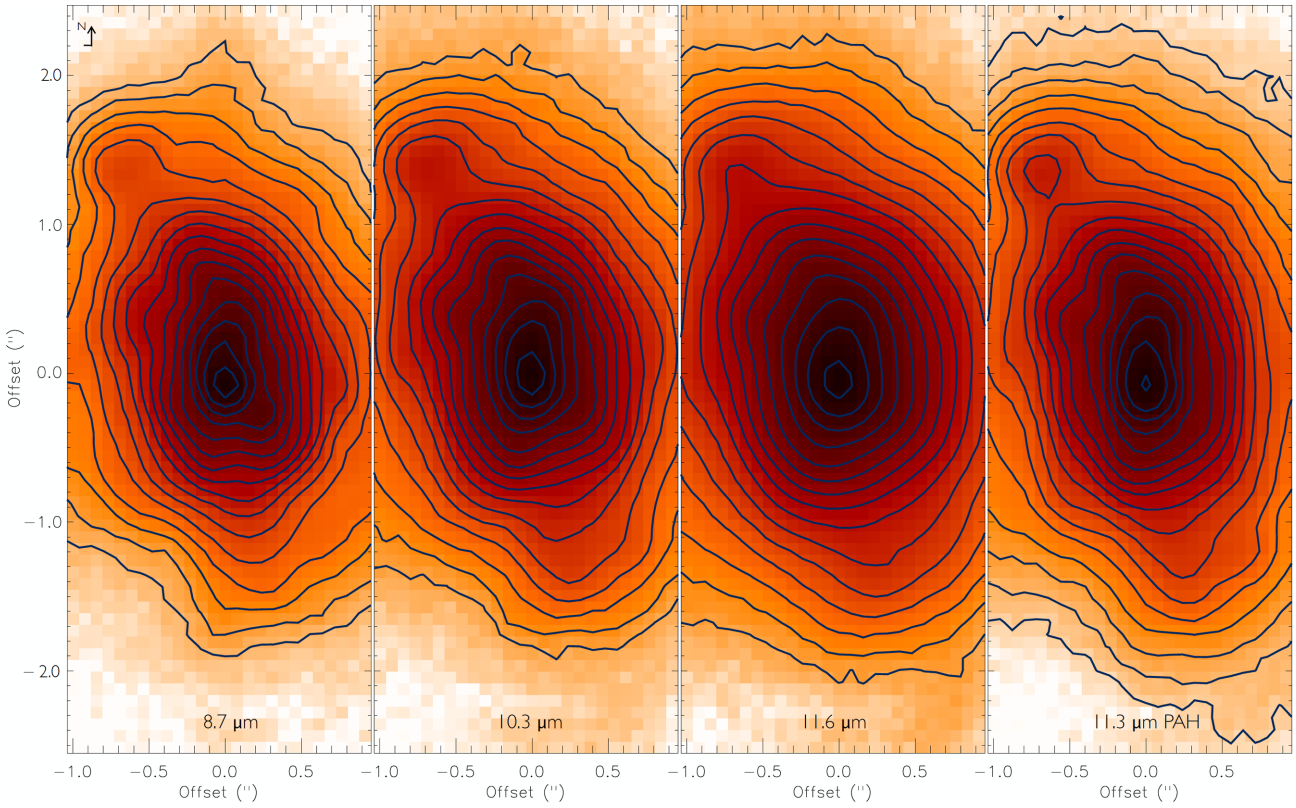

Figure 1. Total flux images of the central 5 arcsec × 2 arcsec (300 pc × 120 pc) at 8.7, 10.3, 11.6 and 11.3 μm PAH. Contours start at 11σ and increase as 1.5^n, where $n = 7, 8, 9, \ldots$, north is up and east is left.

Table 2. Comparison of the nuclear total flux density of NGC 1068 with literature.

λ (μm)	Aperture[a] (arcsec)	Flux density (Jy)	Ref(s).
8.7	2	15 ± 2	a
	3	14.8 ± 1.5	b
	3.8	15 ± 1	b
10.3	2	19 ± 3	a
	3.8	20 ± 2	b
11.3	0.4	16 ± 2	a
	0.4	11.5 ± 1.5	c
11.6	2.0	33 ± 5	a
	1.2	30 ± 5	d
	1.8	39 ± 6	d
	2.0	40 ± 6	d

Notes. [a]Aperture refers to diameter. References: (a) This work; (b) Tomono, Terada & Kobayashi (2006); (c) Jaffe et al. (2004); d) 11.6 μm imaging observations by Mason et al. (2006).

polarization vectors with $P/\sigma_p \geq 3$. At all wavelengths, several polarized features are found:

(i) The most prominent feature is the uniform PA of polarization with an extension of ∼1.5 arcsec × 1 arcsec (90 pc × 60 pc) north of the peak of the total flux density (white crosses in Fig. 2). The PA of polarization is roughly constant, ∼44°, in an area of 1.4 arcsec × 0.8 arcsec (84 pc × 48 pc), with variations of ∼10° (Fig. 3, bottom). In this region, we found a resolved polarized knot at ∼0.4 arcsec (24 pc) north from the peak of the total flux images, termed *'north knot'*. For the *north knot*, the degree of polarization shows a steep increase from south to north, with a peak in the degree of polarization, which then decreases smoothly to the NW and SW directions (Fig. 3, up). The degree of polarization decreases at longer wavelengths (Table 4, Fig. 4) with a constant PA of polarization across the wavelength range.

(ii) The polarized flux images (Fig. 2) show a peak slightly shifted, ∼0.16 arcsec (9.6 pc), SE from the peak of the total flux images. The degree of polarization increases at longer wavelengths with a PA of polarization increasing from 12° ± 10° to 37° ± 5° at 8.7 and 11.6 μm, respectively.

(iii) At ∼0.5 arcsec (30 pc) south from the peak of the total flux images, an extended polarized feature is found. This structure is spatially coincident with the *'SW Lobe'* observed in polarized flux at 2.0 μm using *HST*/NICMOS by Simpson et al. (2002) and in the *K′* band using MMT/MMT-Pol by Lopez-Rodriguez et al. (2015).

We made measurements of the nuclear polarization to compare with the literature (Table 3). In all cases, polarimetric errors were estimated by the variation of the counts in subsets of the data. Our measured nuclear polarization in a 2 arcsec (120 pc) aperture at all wavelengths is higher than the degree of polarization of 1.30 ± 0.05 per cent in a 2 arcsec aperture in the *N* band using the 3.9-m AAT (Lumsden et al. 1999). These authors measured a PA of polarization of 49° ± 3°, which is in marginal agreement with our measurements within the uncertainties. We interpret these results as (1) an increase in the measured degree of polarization by an improvement in the spatial resolution, (2) the mix of different polarization structures within the aperture, and (3) the use of a wide bandwidth within the 10 μm atmospheric window, which implies that their measurements were more strongly affected by the wavelength dependence of the different mechanisms of polarization. We note that the PA of polarization by Lumsden et al. (1999) is in better

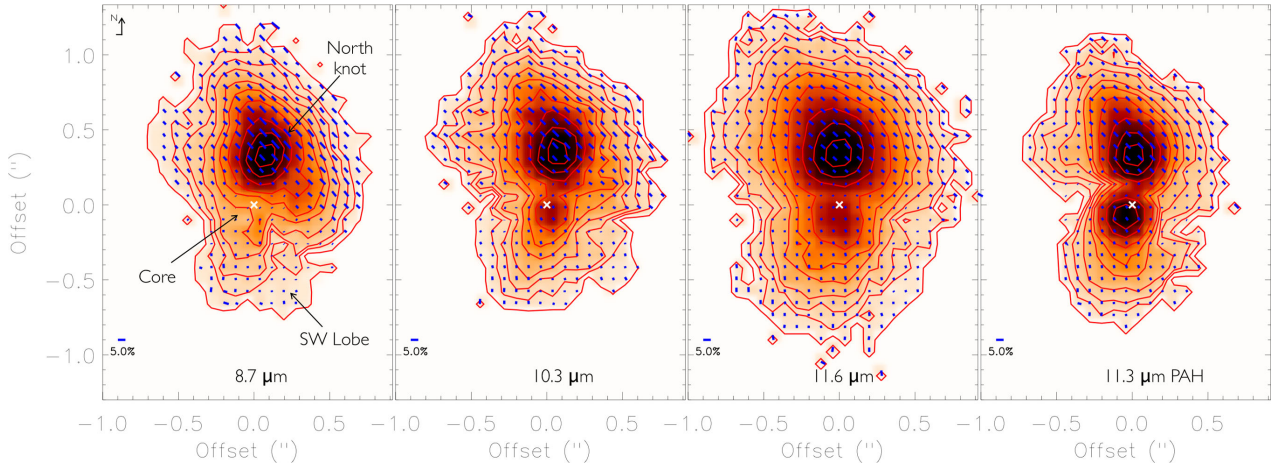

Figure 2. Polarized flux images of the central 3 × 2 arcsec (180 × 120 pc) at 8.7, 10.3, 11.6 and 11.3 μm (PAH) with the overlaid polarization vectors. Contours are plotted in steps of 10 per cent from the peak pixel of the *north knot* where only those polarization vectors with $P/\sigma_P \geq 3$ are shown. A vector of 5 per cent of polarization is shown for scale. The white crosses show the location of the peak of the total flux images (Fig. 1). North is up and east is left.

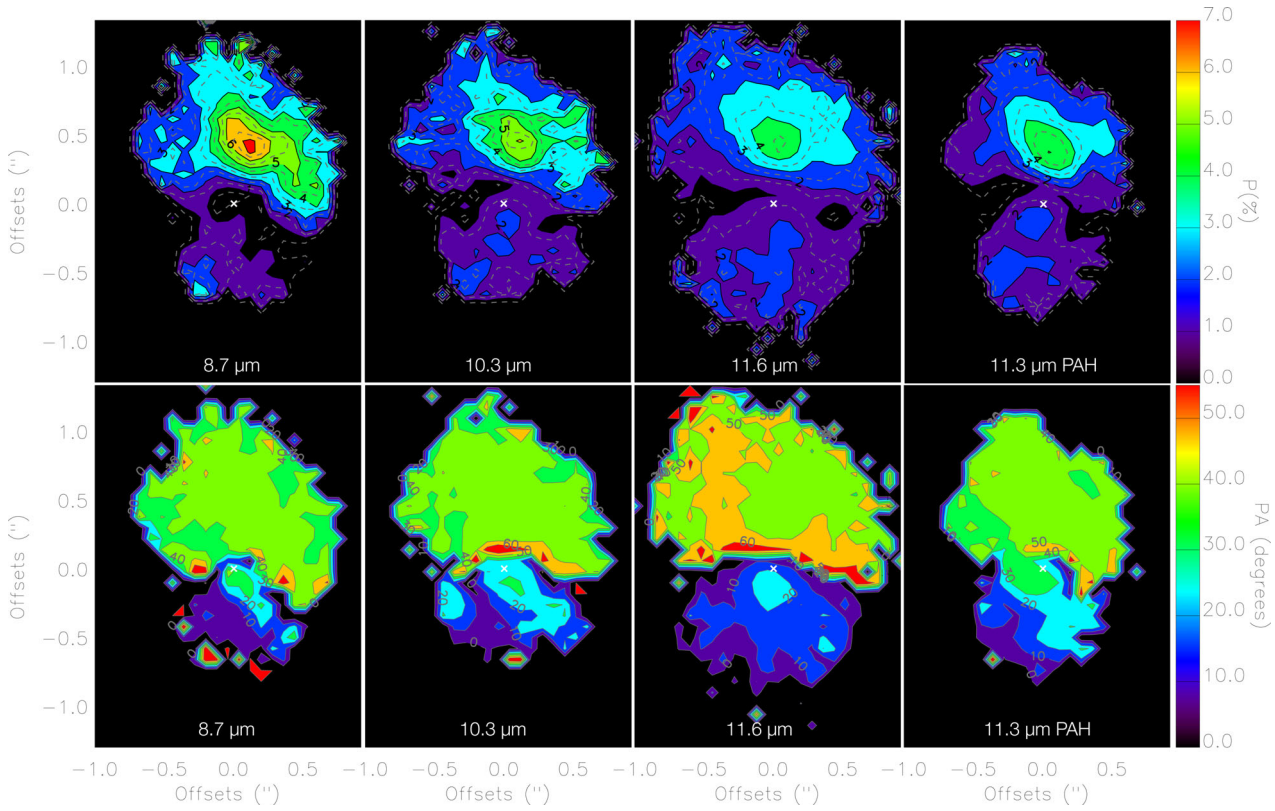

Figure 3. Contours of the degree (first row) and PA (second row) of polarization of the central 3 × 2 arcsec (180 × 120 pc) region at 8.7, 10.3, 11.6 and 11.3 μm (PAH). For the degree of polarization, contours start at 0 per cent and increase in steps of 0.5 per cent. For the PA of polarization, contours are plotted in steps of 10°. The white crosses show the location of the peak of the total flux images (Fig. 1). North is up and east is left.

agreement with our measured PA of polarization in the northern ionization cones (Table 4). This result indicates that their nuclear polarization measurement was dominated by the polarization arising from the northern ionization cone (Section 5.1), as a larger amount of polarized flux is coming from the north regions within their 2 arcsec (120 pc) aperture. Within the nuclear 1.7 × 1.2 arcsec (102 × 72 pc) elliptical aperture, our measured degree of polarization of 2.2 ± 0.7 per cent at 8.7 μm is in excellent agreement with the measured degree of polarization of 2.48 ± 0.57 per cent at 9.7 μm using the 8.1-m Gemini (Packham et al. 2007). We note a difference in the measured PA of polarization of 26.°7 ± 15.°3 at 9.7 μm by Packham et al. (2007), and our measured 46° ± 9° and 53° ± 8° at 8.7 and 10.3 μm, respectively. Both measurements are in marginal agreement within the uncertainties, however we note that the PA of polarization by Packham et al. (2007) is in better agreement with our measurements of the southern polarized feature (Table 4). This difference can be understood as the polarimetric observations of Packham et al. (2007) were more sensitive to the central

Table 3. Comparison of the nuclear polarization of NGC 1068 with literature.

Aperture (arcsec)	λ (μm)	*P* (per cent)	PA (°)	Ref(s).
1.7 × 1.2	8.7	2.2 ± 0.7	46 ± 9	a
	9.7	2.48 ± 0.57	26.7 ± 15.3	b
	10.3	1.8 ± 0.3	53 ± 8	a
	11.3	1.6 ± 0.3	52 ± 5	a
	11.6	1.7 ± 0.3	59 ± 5	a
2	10	1.30 ± 0.05	49 ± 3	c

Note. References: (a) This work; (b) Packham et al. (2007); (c) Lumsden et al. (1999).

Table 4. The measured flux density, degree and PA of polarization and polarized flux for the *southern feature* and *north knot*.

λ (μm)	$F^{(a)}$ (Jy)	*P* (per cent)	PA (°)	$F \times P$ (mJy)
		Southern feature		
8.7	7.0 ± 0.8	0.9 ± 0.3	12 ± 10	63 ± 32
10.3	7.2 ± 0.8	2.1 ± 0.3	33 ± 7	152 ± 41
11.3	10.4 ± 1.2	2.0 ± 0.2	35 ± 3	207 ± 47
11.6	11.2 ± 1.1	1.9 ± 0.2	37 ± 5	213 ± 46
		North knot		
8.7	4.5 ± 0.4	7.0 ± 0.6	40 ± 1	317 ± 48
10.3	6.1 ± 0.6	6.0 ± 0.4	45 ± 1	366 ± 57
11.3	7.2 ± 0.7	5.0 ± 0.4	50 ± 1	362 ± 67
11.6	8.4 ± 0.7	4.5 ± 0.3	45 ± 1	378 ± 59

Note. [a]Flux densities estimated in a 0.4 arcsec (24 pc) aperture centred in the *southern feature* and *north knot*, respectively.

∼1 arcsec due to their low S/N. Our degree and PA of polarization are calibrated to standard stars for polarization measurements, but we note that the total and polarized flux morphologies of the Gemini/MICHELLE polarimetric data by Packham et al. (2007) seem to be rotated by 180° from our data set. We confirmed the CanariCam orientation through comparing our morphology with other total flux measurements, including de-convolved images, and find a high degree of spatial coincidence. We speculate that perhaps the world coordinate system used to indicate north in the Gemini/MICHELLE polarimetric data by Packham et al. (2007) was incorrect, perhaps due to an additional reflection or translation in the polarimetry mode compared to direct imaging.

Based on the observed polarized features and their S/N, we made polarimetric measurements of (1) the *north knot* in a 0.4 arcsec aperture, and (2) the *southern feature* at 0.16 arcsec (9.6 pc) to the peak of the total flux density in a 0.4 arcsec (24 pc) aperture. The total flux density, degree of polarization, PA of polarization and polarized flux density for each feature and filter are shown in Table 4. Fig. 4 shows the measurements (blue squares) for each feature, as well as the used apertures (blue circles in the central panel). We found an aperture dependence on the polarization in the northern ionization cone. Specifically, a constant degree, ∼5 per cent, and PA, ∼44°, of polarization is measured using a 1.4 × 0.8 arcsec (84 × 48 pc) elliptical aperture with PA = 45°.

3.2 Spectropolarimetry

Fig. 4 shows the total flux density (black solid line), the degree and PA of polarization and the polarized flux density (black filled dots) for the PSF-extracted spectra of the 0.4 arcsec (24 pc) fixed aperture spectra of the *north knot* (left), and the *southern feature* (right). The 0.41 arcsec (∼5 pixels) slit (black solid vertical lines) is shown. The total flux spectra were binned to a 0.076 μm (4 pixels) resolution, whilst a 0.285 μm (15 pixels) bin was used for the degree, PA of polarization and polarized flux. The uncertainties were estimated as a variation of the counts within the binned data.

For the *southern feature*, the total flux spectrum shows strong dust continuum emission with a broad silicate absorption feature. This spectrum is similar and consistent with the 0.4 × 0.4 arcsec (24 × 24 pc) slit aperture of the 0.4 arcsec South-South-West (SSW) spectrum using the 8.1-m Gemini by Mason et al. (2006). The degree of polarization slightly increases with increasing wavelength. The PA of polarization slightly increases from 12° ± 10° to 37° ± 5° across the 8–12 μm wavelength range. The polarized flux increases with wavelength.

For the *north knot*, the total flux spectrum is similar to and consistent with the 0.4 arcsec NNE spectrum of Mason et al. (2006), also showing strong dust continuum emission with a broad silicate absorption feature and narrow fine-structure lines. In this spectrum, a [Ar III/Mg VII] blend at 8.99 μm, and a [S IV] fine structure at 10.51 μm are detected. The degree of polarization decreases with increasing wavelength and the PA of polarization is roughly uniform through the spectrum. The polarized flux increases with increasing wavelength.

Aitken et al. (1984) measured a uniform degree, 1.29 ± 0.09 per cent, and PA, 54°.8 ± 1°.9, of polarization across the 8–13 μm wavelength range using a 4.2 arcsec (252 pc) beam. We note that their measured PA of polarization is consistent with the PA of polarization of the northern ionization cone measured in our observations. We thus gather that the measurements of Aitken et al. (1984) were dominated by the northern ionization cone within their 4.2 arcsec (252 pc) beam, as a larger amount of polarized flux is coming from the north regions within their beam. This result makes it difficult to obtain information about the core of NGC 1068, and shows the potential of subarcsecond resolution polarimetric MIR observations to obtain more sensitive observations with the aim to study the cores of AGNs.

4 POLARIZATION MODEL

We aim to reproduce the observed polarization in the 7.5–13 μm wavelength range of the several observed features discussed in Section 3. Specifically, we wish to reproduce the observed degree and PA of polarization for (1) the northern and southern ionization cones, and (2) the obscuring dusty structure.

4.1 Components of the polarization model

MIR spectropolarimetric observations of 55 objects (e.g. young stellar objects, star formation regions and active galactic nuclei) using 4-m class telescopes found that 90 per cent of the objects can be explained by dichroism (Smith et al. 2000). Dichroic extinction and emission can compete at a given wavelength. Both mechanisms need to be disentangled through a multiwavelength study. Fortunately, some dust grain features, such as silicates, are present in the MIR wavelength range, and can be used to distinguish between the two mechanisms. In the case of silicates, the absorptive polarization shows a peak at ∼10 μm, while the emissive polarization is less structured. In general, if a rotation of the polarization angle with wavelength is observed, then more than one mechanism of polarization may be present. Unless the several polarization mechanisms

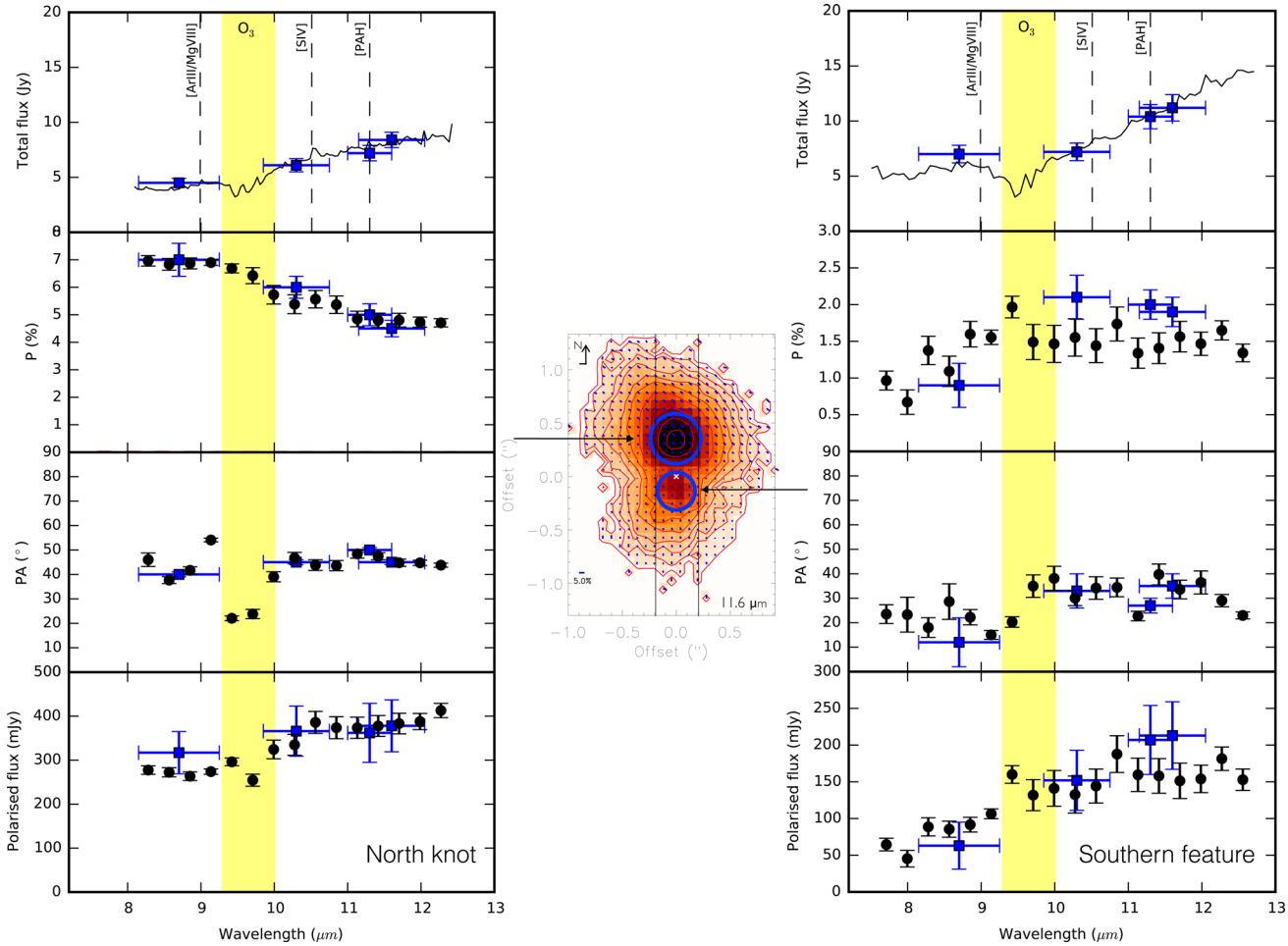

Figure 4. The measured total flux density and polarization of the *north knot* (left) and *southern feature* (right). The polarized flux image (centre) with overlaid polarization vectors at 11.6 μm as in Fig. 2 is shown. The blue circles in the central panel represent the aperture used for the imaging polarimetric measurements (Section 3.1.2), and the two vertical black solid lines demarcate the position and width of the 0.41 arcsec (∼5 pixels) slit. The total flux density (first row) spectra (black solid line) and imaging (blue squares) measurements are shown with a spectral bin of 0.076 μm (4 pixels). The dashed lines indicate the positions of the [Ar III/Mg VII] blend at 8.99 μm, [S IV] fine-structure at 10.51, and 11.3 μm PAH emission lines, whilst the yellow region shows the approximate extent of the telluric O_3 band. The degree (second row), PA (third row) of polarization and polarized flux density (fourth row) of the imaging (blue squares) and spectropolarimetric (black circles) observations are shown. The spectropolarimetric observations have a spectral bin of 0.285 μm (15 pixels).

have intrinsically the same polarization angle, the net polarization angle will be a function of wavelength. Both the degree and angle of polarization profiles are crucial to investigate the emissive and absorptive polarization components at MIR wavelengths.

The dichroic components can be disentangled following the procedure put forward by Aitken et al. (2004). These authors presented a procedure to separate and identify the absorptive, p_a, and emissive, p_e, polarization components within the 7.5–13 μm wavelength range. The emissive polarization component is given by $p_e = |p_a/\tau_\lambda|$, where τ_λ is the wavelength-dependent extinction curve. This condition can be used as long as the difference in orthogonal optical depths of the dust grains is less than unity for p_a, which makes p_a independent of the optical depth. This situation will hold if $\tau_{MIR} <$ a few tens. For the extinction curve, the standard silicate-graphite interstellar dust grain of $R_v = 5.5$ is assumed,[4] which appears to be in agreement with the MIR extinction at different sightlines through the Galactic centre (Weingartner & Draine 2001). Variations in our model of less than 2 per cent are found when extinction curves of $R_v = 2.1$, and 3.1 were used. For the absorptive component, p_a, we took the Becklin–Neugebauer (BN) object in Orion (Aitken, Smith & Roche 1989) because it is the best-defined absorptive component with the highest S/N, and commonly used in these studies (Smith et al. 2000).

The polarization model to separate the absorptive and emissive polarization components is constructed as follows. It assumes an emission source that can be either polarized or unpolarized, and which is viewed through a cold dichroic sheet of dust grains. The Stokes parameters from both components simply add up, and the observed Stokes parameters, q_{obs} and u_{obs}, can be fitted as a linear combination of both components:

$$q_{obs} = q_a + q_e = Ap_a + Bp_e \quad u_{obs} = u_a + u_e = Cp_a + Dp_e \qquad (1)$$

where A, B, C and D are the constants used for the fitting procedure. We followed the fitting procedure described by Aitken et al. (2004).

[4] Note that recent studies (Gao, Li & Jiang 2013) suggested that a trimodal grain size distribution with a combination of $R_v = 2.1$, 3.1 and 5.5 is required to achieve a good fit to the extinction curve of the Galactic centre from the UV to the MIR.

Then, the final degree of polarization, $P_{\rm obs} = \sqrt{q_{\rm obs}^2 + u_{\rm obs}^2}$, and the position angle, $\mathrm{PA}_{\rm obs} = 0.5 \arctan(u_{\rm obs}/q_{\rm obs})$, are estimated.

The total flux spectrum is defined as an extinguished blackbody component with a characteristic temperature $T_{\rm BB}$. We have assumed an extinction curve with $R_{\rm v} = 5.5$, and the characteristic temperature was sampled in steps of 10 K. The polarized flux was estimated as the modelled total flux, times the total degree of polarization, $P_{\rm obs}$.

4.2 Fitting of the ionization cones

In the case of the northern ionization cone, a constant PA of polarization (Table 4, Fig. 4, left) suggests a unique polarization mechanism. In objects in our Galaxy where MIR polarization arises through dichroic absorption by aligned dust grains, a prominent silicate peak in the degree of polarization is present just longwards of 10 μm (i.e. Aitken et al. 1986; Smith et al. 2000). No such feature is present in the polarization spectrum of the *north knot* in NGC 1068, which instead shows a slow decrease in the degree of polarization with increasing wavelength. Thus, non-silicate features, i.e. non 9.7 μm feature, are present in the MIR polarization. We give a further interpretation of these features in Section 5.1.

In the southern ionization cone, the rotation of the PA of polarization (Table 4, Fig. 4, right) suggests that more than one mechanism contributes to the polarization. Following the procedure described in Section 4.1, we simultaneously fit the measured total flux, degree and PA of polarization of the *southern feature* (Fig. 5). The polarization model has four free model parameters: (1) the visual extinction $A_{\rm v}$ towards the core, (2) the blackbody characteristic temperature $T_{\rm BB}$, (3) the degree of polarization and (4) the PA of polarization. The fit was considered acceptable when the reduced χ^2 was minimized. We obtain a reduced $\chi^2 = 0.21, 2.22, 15.8$ and 14.2 for the flux density, degree and PA of polarization, and polarized flux density, respectively. Although we are aware of the limitations of the χ^2 fitting procedure, we are more interested on explaining the overall behaviour of the polarization spectrum rather than optimize the goodness of the fitting, as we are limited by the low S/N of the observations. Further development of a Bayesian fitting procedure is out of the scope of this paper, but we think it will benefit the statistical analysis presented here as shown by Lopez-Rodriguez (2016). For the best fit, we found a blackbody component with a characteristic temperature of $T_{\rm BB} = 210 \pm 10$ K, extinguished with $A_{\rm v} = 9 \pm 1$ mag. The emissive polarization component is dominant and describes the observed wavelength dependence of the degree of polarization with a PA $= 35^\circ \pm 1^\circ$. The absorptive component contributes <20 per cent of the polarization with a PA $= 127^\circ \pm 1^\circ$. We give a further interpretation of this feature in Section 5.2.

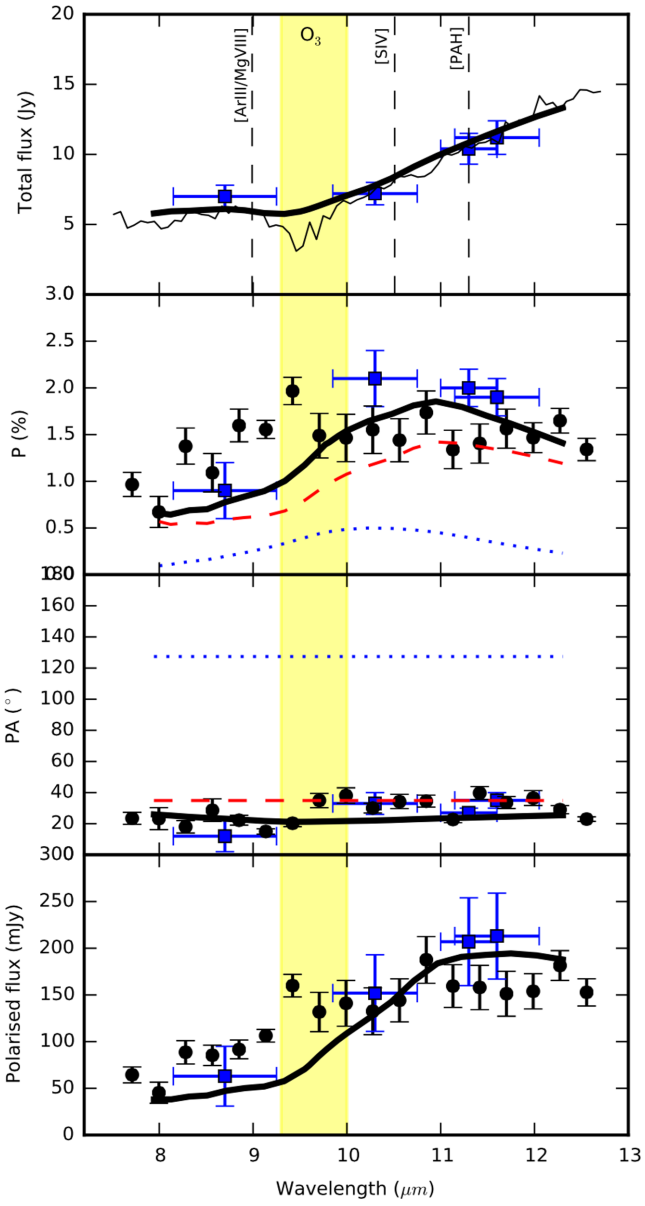

Figure 5. *Southern feature* measurements as in Fig. 4, with the total model (black solid line), and the absorptive (blue dotted line) and emissive (red dashed line) polarization components from our polarization model presented in Section 5.2.

4.3 Fitting of the dusty central structure

We now investigate the expected MIR polarization of the obscuring dusty structure in terms of dichroism. Dichroic absorption is the dominant mechanism of polarization at NIR wavelengths in the core of NGC 1068. This allows us to constrain the absorptive and emissive polarization components in the 2–13 μm wavelength range. For the absorptive component, we assume a Serkowski (Serkowski, Mathewson & Ford 1975) curve up to 8 μm, followed by the absorptive profile of the BN object in Orion (Section 5.2.1) in the 8–13 μm wavelength range. This composition takes into account the silicate feature at MIR wavelengths, that, if not used, would lead to the expected MIR polarization being underestimated by a factor >100. Using NIR polarimetric adaptive optics observations, Lopez-Rodriguez et al. (2015) estimated an intrinsic (starlight-corrected) polarization at K' of 7.0 ± 2.2 per cent in a 0.5 arcsec (30 pc) aperture. Using this value to constrain the absorptive polarization allows us to estimate the intrinsic polarization of the obscuring dusty structure in NGC 1068. To constrain the extinction curve (with $R_{\rm v} = 5.5$ as in Section 5.2.1), lower and upper limits of the visual extinction towards the core of NGC 1068 must be assumed. For the upper limit we used $A_{\rm v} = 39$ mag (Packham et al. 1997; Watanabe et al. 2003; Lopez-Rodriguez et al. 2015), interpreted as the extinction to the NIR emitting regions. For the lower limit, $A_{\rm v}$ is estimated using the 9.7 μm silicate feature, $\tau_{9.7\,\mu\rm m} \sim 0.41$, of the nuclear spectrum in a 0.4 × 0.4 arcsec (24× 24 pc) slit aperture by Mason et al. (2006).

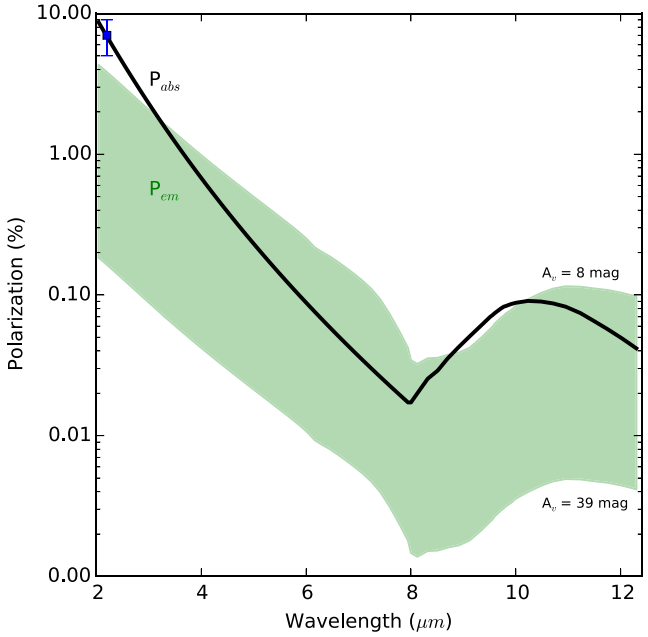

Figure 6. Expected absorptive ($P_{\rm abs}$, black solid line) and emissive ($P_{\rm em}$, green shaded area) intrinsic polarization from the obscuring dusty structure surrounding the central engine of NGC 1068. The absorptive polarization was scaled to the intrinsic polarization at K' (blue dot) of 7.0 ± 2.2 per cent estimated by Lopez-Rodriguez et al. (2015).

This result was then converted[5] to $A_{\rm v} \sim 8$ mag. The difference of both visual extinctions can be interpreted as a temperature gradient and inhomogeneities (clumpiness) in the obscuring dusty material (i.e. Pier & Krolik 1992; Imanishi & Ueno 2000; Levenson et al. 2007).

With the constraints on each component given above, we estimated the absorptive and emissive intrinsic polarization of the obscuring dusty structure of NGC 1068 in the 2–13 μm wavelength range (Fig. 6). At wavelengths <4 μm, the absorptive component is dominant for all values of $A_{\rm v}$. The emissive component is dominant for low values of the visual extinction in the wavelength ranges of ∼4–8 μm and >11 μm, while both absorptive and emissive components compete in the ∼8–10 μm wavelength range. Based on this model, the expected polarization from extrapolating the NIR absorptive component is $\lesssim$0.1 per cent in the 8–13 μm wavelength range. We note that while there could be a component of polarized emission from those dust grains, if they are sufficiently warm to emit in the MIR, the uncertainties in estimating any contribution are very large. We give a further interpretation of this feature in Section 5.3.

5 ANALYSIS AND DISCUSSION

We outline the general physical structure of the central 100 pc of NGC 1068, which will aid us in the analysis of the several observed polarization features introduced in Section 3. The polarized structures are discussed in the following order: (1) the northern ionization cone, (2) the southern ionization cone and (3) the obscuring dusty structure.

[5] The conversion of the 9.7 μm silicate feature to visual extinction is $A_{\rm v} = 18.5\,\tau_{9.7\,\mu{\rm m}}$ (Roche & Aitken 1984).

We present the structure of the inner 100 parsecs of NGC 1068. It shows a complex geometry in the inner few parsecs. Through 5 and 8.5 GHz radio observations using the very long baseline array, Gallimore et al. (2004) detected the location of the hidden active nucleus (labelled as S1 in their paper) as a parsec-sized (∼0.8 pc diameter) structure with a major axis at PA ∼105°. The emission of this component most likely indicates strong free–free emission from hot (10^4–10^5 K) ionized gas. This structure is oriented nearly perpendicular to the inner radio jet axis, PA ∼12° (Gallimore, Baum & O'Dea 1996). The kinematics of the maser clouds indicate that the masers are located in a non-Keplerian disc with inner radius ∼0.65 pc and outer radius ∼1.1 pc at a PA of −40° (Gallimore et al. 2001). Through MIR interferometric observations, Jaffe et al. (2004) estimated a warm ($T = 320$ K) dust structure with a 2.1 pc thick and 3.4 pc diameter, surrounding a hot ($T > 800$ K) compact (∼1 pc) structure. Additional MIR interferometric observation by Raban et al. (2009) suggested a hot (∼800 K) 1.35 pc long and 0.45 pc thick structure with a larger 3 × 4 pc and warm ($T \sim 300$ K) dust structure at a PA = −42°. These authors suggested that the dust and the maser disc are co-spatial, where the dusty torus begins at the outer edge of the maser disc. These results are consistent with the established relationship between the water maser excitation and warm (>600 K) molecular dust in AGNs (Neufeld, Maloney & Conger 1994). Where the maser disc ends and the dusty torus structure begins may be more a question of semantics rather than a true physical boundary. Another implication from their results is that as the masers are seen edge-on, so is the torus, consistent with the classification of NGC 1068 as a type 2 AGN. A sketch of the inner few parsecs of NGC 1068 is shown in Fig. 7, left. Note that this figure is a detailed sketch of the central parsec of NGC 1068 adapted from fig. 6 in Lawrence & Elvis (2010). Based on the geometry of the inner few parsecs, misalignments between these structures are found. Although misaligned structures on similar spatial scales have been observed in other AGNs (i.e. Miyoshi et al. 1995; Wilson, Braatz & Henkel 1995; Greenhill et al. 1997; Hagiwara et al. 1997; Trotter et al. 1998), it is not the scope of this paper to investigate these, and we refer to the reader to the discussion in Lawrence & Elvis (2010).

At larger scales (>10 pc), NGC 1068 displays a variety of structures. Most of the radiation emerges from the interaction of the radio jet with material in the ionization cones partially extinguished by the disc of the galaxy and/or the NIR bar. The inner few parsecs of the ionization cone are roughly aligned with the radio jet in the N–S direction. At ∼24 pc in the northern ionization cone, the radio jet changes direction when it interacts with the molecular cloud (i.e. *north knot*; e.g. Gallimore et al. 2001). The radio jet emission between the central few parsecs and the molecular cloud is dominated by synchrotron emission, while the jet–molecular cloud interaction radiates at all wavelengths. After this interaction, the radio jet expands and is roughly aligned with the extended northern ionization cone on a ∼50–100 pc scale. The radio jet in the southern ionization cone does not change direction and moves away from our LOS. The radio jet and molecular cloud are extinguished by the NIR bar with an extension of ∼1.92 kpc at a PA ∼48° (Scoville et al. 1988; Schinnerer et al. 2000; Emsellem et al. 2006). Fig. 7, right outlines the large-scale structures.

5.1 The northern ionization cone

We analyse here the polarization mechanism from the northern extended polarization feature, and the *north knot*. As we noted in the Introduction, NGC 1068 has an NIR bar with an extension of

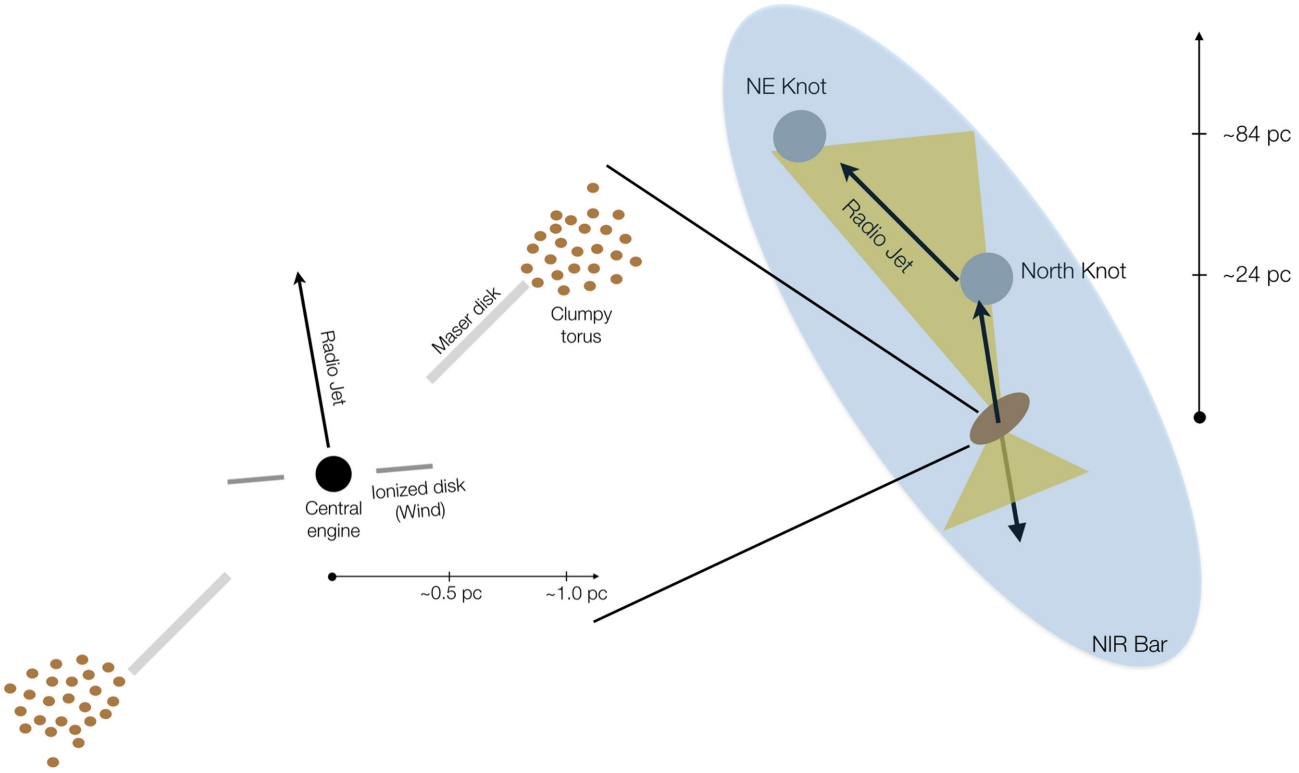

Figure 7. Sketch of the central 100 × 100 pc (right-hand panel) with a zoom-in of the central few parsecs (left-hand panel) of NGC 1068 (both panels are not on linear scale). In the central few parsecs (left-hand panel): the central engine (central black dot), the ionized disc/wind (dark grey region) occupying the inner ∼0.4 pc (Gallimore, Baum & O'Dea 2004), the maser disc (light grey region) from ∼0.6 pc to ∼1.1 pc at PA = −40° (Gallimore et al. 2001), the obscuring dusty material (brown dots) up to ∼1.35 pc at PA = −42° (Raban et al. 2009) and the radio jet (black solid arrow) at PA ∼ 10° (Gallimore et al. 2004) are shown. In the 100 × 100 pc scale (right-hand panel): the central few parsecs are represented as a brown ellipsoid with the PA of the obscuring dusty material. The inner radio jet at PA ∼ 10° is shown as a black arrow, bending to PA ∼ 40° after interaction with the *north knot* (grey circle), towards the NW knot (grey circle). The [O III] ionization cones (yellow polygons) and the NIR bar (light-blue ellipse) are shown. North is up and east is left.

32 arcsec (1.92 kpc) at a PA = 48° (Scoville et al. 1988; Schinnerer et al. 2000; Emsellem et al. 2006). In this region, the optical (Scarrott et al. 1991) and, *J* and *H* (Packham et al. 1997) polarization shows a PA of polarization consistent with the orientation of the NIR bar. This result is most easily interpreted as polarization arising from extinguished starlight passing through aligned dust grains in the NIR bar. Dichroic absorption dominates the polarization in the NIR bar, suggesting that the dust grains are aligned by the galactic magnetic field at PA = 48°. The measured PA of polarization of ∼44° in the northern ionization cone is consistent with the measured PA of polarization in the optical, *J* and *H* bands. This result suggests that the dichroic absorption mechanism may dominate from the optical to the MIR in the NIR bar at the northern ionization cone.

To understand the polarization of the *north knot* and its relation with the extended polarization feature, we further compare the degree of polarization map at 8.7 μm, and maps of the emission lines Paschen α (Paα) at 1.875 μm (Fig. 8, middle) and [O III] at 0.5007 μm (Fig. 8, right). We obtained archival images of NGC 1068 at Paα (ID: 7215, observed on 1998 Feb. 21) and [O III] (ID: 5754, observed on 1995 Jan. 17) emission lines using *HST*. We found that the MIR polarization is spatially coincident with the Paα (Fig. 8, middle) and [O III] (Fig. 8, right) emission lines. Paα line emission can be interpreted as a tracer of young (<30 Myr) star formation or gas emission. Storchi-Bergmann et al. (2012) found an episode of young (30 Myr) stellar population in a ring-like structure at ∼100 pc from the nucleus, coincident with the ring of molecular gas detected in the 2.12 μm warm molecular hydrogen line and in cold molecular gas detected by ALMA (García-Burillo et al. 2014). We found that the morphology of this young stellar population and cold molecular gas resembles neither the Paα line emission nor the MIR features in the northern ionization cone. Additionally, we found no evidence of 11.3 μm PAH feature in the northern ionization cone in our spectropolarimetric observations (Fig. 4, left), consistent with MIR spectroscopic observations by Mason et al. (2006). This comparison between Paα line emission with the degree of polarization suggests that the Paα line emission is tracing gas photoionized by the AGN and/or gas excited by shocks in the ionization cones. This result is further supported by the spatial correspondence of Paα and [O III] emission lines, as the latter is a good tracer of the gas emission in the narrow-line regions (e.g. Evans et al. 1991; Emsellem et al. 2006; Kraemer et al. 2015). Based on these results, we interpret the MIR polarization of the northern ionization cone as arising from extinguished radiation from dust and gas heated by the AGN (e.g. Crenshaw & Kraemer 2000; Kraemer & Crenshaw 2000a; Das, Crenshaw & Kraemer 2007) and the interaction of the jet (e.g. Gallimore et al. 1996) with dust and gas in the northern ionization cone passing through the aligned dust grains in the NIR bar producing the uniform PA of polarization in the northern ionization cone. The fact that the PA of polarization is not perfectly aligned along the PA of the NIR bar can be explained as the radiation from the jet–molecular cloud interaction being polarized with a slightly different PA of polarization. Variations of the S/N in

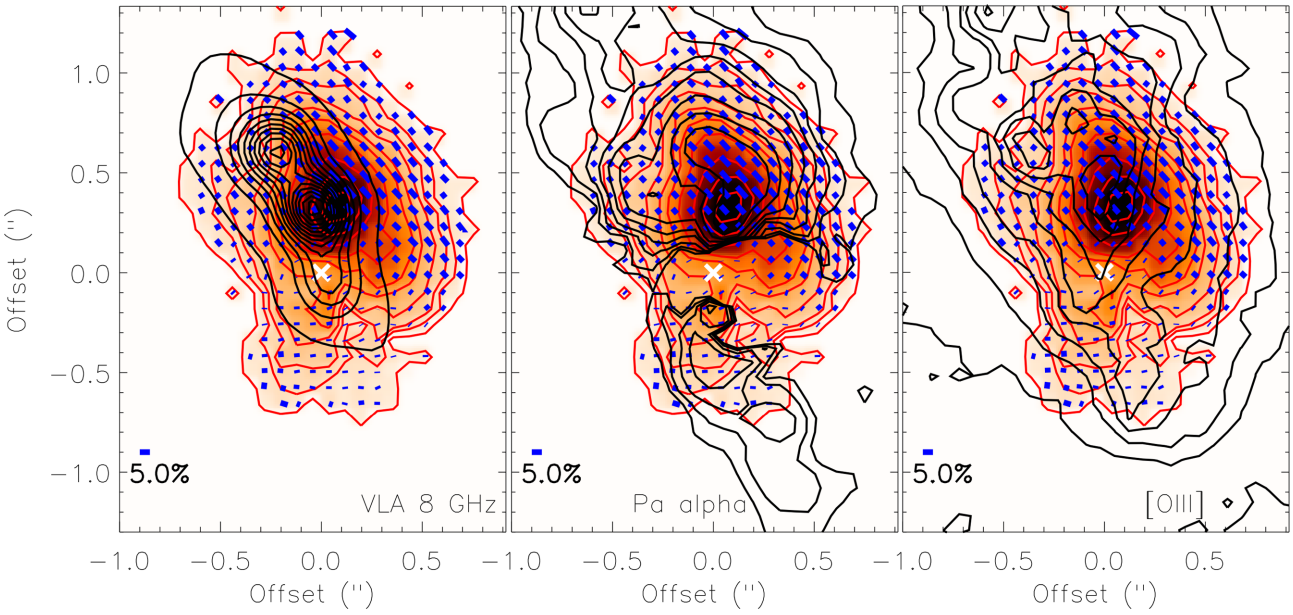

Figure 8. The 3 arcsec × 2 arcsec (180 pc × 120 pc) central region of NGC 1068 showing the polarized flux image with overlaid polarization vectors at 8.7 μm (as in Fig. 2) with overlaid contours of VLA 8 GHz (left), Pa α (middle) and, [O III] (right) lines emission. For VLA 8 GHz, contours start at 5σ and increase in steps of 50σ. For Pa α, contours start at 3σ and increase in steps of 3σ. For [O III], contours star at 8σ and increase as $2^n\sigma$, with $n = 4, 5, 6, \ldots$. North is up and east is left.

the northern regions can also explain the ∼10° fluctuations of the PA of polarization.

Based on the model presented in Section 4, the dust grains in the northern ionization cone are different from those in the interstellar medium (ISM) in the Milky Way. This confirms the spectropolarimetric observations of Aitken et al. (1984), who also found a relatively featureless polarization spectrum in a 4.2 arcsec (252 pc) beam. They concluded that it was not produced by standard silicate grains. The *north knot* region produces the bulk of the nuclear polarization in NGC 1068, and our observations confirm that it mostly arises from non-silicate grains, despite the clear signature of silicate absorption in the total flux density spectrum (Fig. 4, left).

We considered other polarization mechanisms to explain the MIR polarimetric observations of the northern ionization cone. Scattering off electrons and/or dust grains can be ruled out due to the uniform PA of polarization in this region; there is no evidence of a centrosymmetric pattern that would be expected for scattering of radiation from a nuclear source. We considered also the possibility of the jet–molecular cloud interaction as a dust grain alignment mechanism in the northern ionization cone. For this study, we obtained archival images of NGC 1068 at 8 GHz (Observer: AC467, observed on 1999 Sep. 08) using the Very Large Telescope (VLA). We plot the degree of polarization map at 8.7 μm and radio emission at 8 GHz in Fig. 6, left. If the jet–molecular cloud interaction dominated in the northern ionization cone, we would expect the magnetic field to be parallel to the interface of the jet–molecular cloud interaction (e.g. Drury 1983). The magnetic field is compressed in the interface and increases in strength, resulting in better dust grain alignment in the northern ionization cone than in the ISM. As noted in Section 5, the jet bends at the position of the *north knot*, which would imply variations of PA of polarization of ∼30° as a consequence of the different interface between jet and surrounding molecular dust in the northern ionization cone. Despite the registration uncertainties of ∼0.1–0.3 arcsec in Fig. 6, left, the uniform PA extends further (∼1.5 × 1.0 arcsec, i.e. 90 × 60 pc) than the radio jet emission. These observations suggest that the jet–molecular cloud interaction cannot be the dominant polarization mechanism in the whole northern ionization cone.

5.2 The southern ionization cone

We present here an analysis of the southern ionization cone and its *southern feature*. The optical and NIR spectral lines and continuum emission are much fainter to the south of the core of NGC 1068 (Macchetto et al. 1994; Bruhweiler et al. 2001; Thompson et al. 2001, see also Fig. 6), with a deeper silicate feature, $\tau_{9.7}$, within 1 arcsec SSW of the core (Mason et al. 2006). To show these results, we produced (Fig. 9) an NIR colourmap of NGC 1068 using archival *HST*/NICMOS images, specifically *F*110*W* and *F*160*W* (ID: 7215, observed on 1998 Feb. 21). Next, we modelled the PSF at each filter using TinyTim (Krist, Hook & Stoehr 2011), and then the PSFs were subtracted from the *HST*/NICMOS images. Finally, the *F*110*W*/*F*160*W* colourmap (Fig. 9) was produced. Fig. 9 shows larger amount of host galaxy dust to the south of the core of NGC 1068, suggesting that the southern ionization cone suffers from higher extinction than the northern ionization cone. This result is in agreement with the increase of the NIR polarization to the SW (Young et al. 1995; Packham et al. 1997; Simpson et al. 2002; Lopez-Rodriguez et al. 2015), interpreted as an additional scattering medium in this region. In addition, the dusty disc of the galaxy has an inclination of 29° (García-Gómez, Athanassoula & Barberà 2002), screening the southern but not the northern ionization cone (e.g. Packham et al. 1997; Bock et al. 1998; Kraemer & Crenshaw 2000b). Thus, the southern ionization cone is more extinguished than the northern one, as is also suggested by the deeper silicate feature (Mason et al. 2006).

We found that the MIR polarization of the southern ionization cone is spatially coincident with the Pa α (Fig. 8, middle) and [O III]

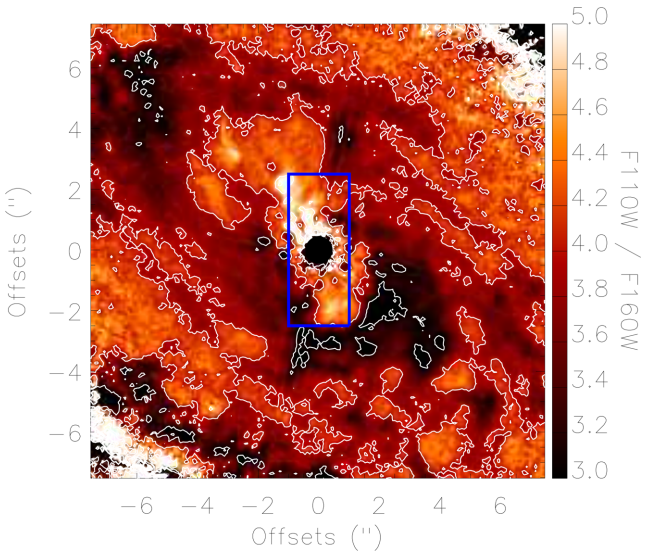

Figure 9. *F*110*W*/*F*160*W* colour map of the 15 arcsec × 15 arcsec (900 pc × 900 pc) central region of NGC 1068. Contours start at 3σ and increase as 1σ. The NIR images were PSF subtracted using TinyTim, then the colourmap was produced. The central 0.4 arcsec (24 pc) was masked (black filled circle) due to the noise pattern produced by the PSF subtraction. The FOV (5 arcsec × 2 arcsec, 300 pc × 120 pc) of the MIR observations (blue rectangle) is shown.

(Fig. 8, right) emission lines. The PA of polarization (Fig. 3, bottom) is ∼30° along the Paα emission (Fig. 8, middle), whereas a PA of polarization of ∼10° is observed where not spatial coincident with this emission line is found. For those regions where MIR polarization and Paα emission are spatially coincident, we interpret the observed polarization in the southern ionization cone as dust directly heated by the jet; this dust emission passes through both the NIR bar and the disc of the galaxy. For those regions where MIR polarization and Paα emission are not spatially coincident, the polarization arises from dichroic absorption in the galaxy. As the southern ionization cone is affected by several extinction components, its PA of polarization differs from that observed in the northern regions.

As in the northern regions, scattering off electrons and/or dust grains can be ruled out, as there is no evidence of the centrosymmetric pattern that would be expected for scattering of radiation from a nuclear source. If the radio jet were responsible for the dust grain alignment, then a constant PA of polarization would be expected. Such a uniform polarization pattern is however not observed, and thus polarization arising from dust emission of aligned dust grains by the radio jet can be ruled out.

5.2.1 *The* southern feature

Based on the model presented in Section 4.2, we interpret the polarization of the *southern feature* as a polarized dust emission component passing through a large concentration of silicates as well as the dusty disc of the galaxy along our LOS. The polarized dust emission component in the *southern feature* can arise from (1) magnetically aligned dust grains directly heated by the jet in the southern ionization cone close to the AGN, or (2) aligned dust grains in the obscuring dusty structure surrounding the central engine (Section 5.3). As the core is included within the aperture used to perform the measurements of the *southern feature*, we cannot distinguish between dust grains in the southern ionization cone and those grains associated with the circumnuclear dusty obscuring structure. Unfortunately, to obtain polarimetric measurements in an aperture further south of the nucleus to avoid the core of NGC 1068 produced low S/N spectra making it difficult to interpret the polarization.

As noted in Section 4, a prominent peak at wavelengths ∼10 μm would be present in the degree of polarization if silicate grains were present. It is interesting that the polarization of the *southern feature* can be reproduced with silicate emission/absorption, while the *north knot* does not show such silicate feature in the polarization spectrum. This suggests different dust composition within the central 120 pc of NGC 1068. If the interaction of the jet with the dust in the northern ionization cone is changing the dust properties, then the observed silicate feature of the *southern feature* may favour the observed polarization arising from dust grains in the obscuring dusty structure surrounding the central engine of NGC 1068. We study the contribution of the obscuring dusty structure in Section 5.3.

5.3 The obscuring dusty structure

Although the MIR total flux density peaks at the position of the AGN (i.e. Braatz et al. 1993; Cameron et al. 1993; Lumsden et al. 1999; Bock et al. 1998; Alloin et al. 2000; Bock et al. 2000; Tomono et al. 2001; Jaffe et al. 2004; Galliano et al. 2005; Mason et al. 2006; Tomono et al. 2006; Raban et al. 2009; López-Gonzaga et al. 2014), a very low polarization with an upper limit of 0.3 per cent at this location is detected within the 8–13 μm wavelength range (Figs 2 and 3). We present here an interpretation of the MIR polarization of the obscuring dusty structure of NGC 1068 in the context of the CLUMPY[6] torus models (Nenkova, Ivezić & Elitzur 2002; Nenkova et al. 2008a,b). CLUMPY models the obscuring dusty structure as an optically and geometrically thick torus surrounding the central engine of an AGN, and comprised of dusty clouds.

Lopez-Rodriguez et al. (2015) interpreted the NIR polarization of NGC 1068 in terms of the level of magnetization through the estimation of the thermal-to-magnetic pressure ratio in the clumps. Specifically, the NIR polarization they measured is determined in the outermost material of lower optical depth in the clumps. Based on these results, and the fact that the absorptive/emissive polarization components should arise from the same aligned dust grains, but with orthogonal polarization angles, we are able to give an interpretation of the IR polarization. The NIR polarization arises from the passage of NIR radiation from directly illuminated clumps through the low-density dusty regions of the clumps with a visual extinction of $A_{\rm v}^{\rm NIR}$. The same aligned dust grains emit at MIR wavelengths, and this radiation passes through lower extinction, $A_{\rm v}^{\rm MIR}$, than the NIR photons. The lower the extinction, the higher the emissive intrinsic polarization component, i.e. $P_{\rm em} = P_{\rm abs}/\tau$. Since our observations do not show an MIR polarization at the core, and from our polarization model, the minimum visual extinction that the MIR radiation passes through is $A_{\rm v}^{\rm MIR} = 8$ mag. For lower $A_{\rm v}^{\rm MIR}$, a degree of polarization higher than 0.1 per cent is expected (Fig. 6), which would be detectable in our observations. Thus, the model of emissive polarization arising from aligned dust grains in the clumps is consistent with the non-detection of MIR polarization at the core of NGC 1068. Based on these results, Fig. 10 shows the possible configuration for a clump compatible with the observations.

[6] CLUMPY models can be found at: www.clumpy.org

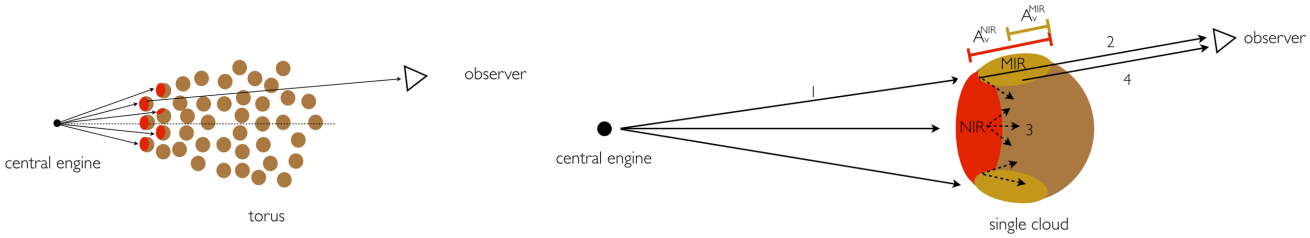

Figure 10. Sketch of the clumpy models (left), and clump configuration (right) compatible with the observed IR polarization. (1) The innermost clump is directly irradiated by the central engine and re-emits in the NIR from the directly illuminated face of the clump. Then, (2) the NIR radiation passes through the low-density regions of the dusty clump, towards the observer. Polarization arises from dichroic absorption through a visual extinction $A_{\rm v}^{\rm NIR}$. (3) The radiation going through higher density regions is completely extinguished. (4) The shielded outer layer of the clump emits in the MIR, and MIR polarization arises from dichroic emission at the low-extinction regions, $A_{\rm v}^{\rm MIR}$, of the outer layer of the clump.

Although the CLUMPY models assume only discrete dust clumps with no interclump medium, an interclump medium should be considered as a more physical realistic model. We here put constraints on the extinction of the interclump medium to be used in two-phase clumpy torus models. Assuming a magnetohydrodynamical framework in the obscuring dusty structure of NGC 1068 (Lopez-Rodriguez et al. 2015), a global magnetic field at the same location of the obscuring dusty material aligns the dust grains in both the interclump medium and in the clumps. In this scheme, the IR polarization can arise from the passage of radiation through aligned dust grains in the clumps, as described above, and/or in the interclump medium. To obtain an upper limit on the extinction of the interclump medium, we assume that the clumps are optically thick with uniform density, then the aligned dust grains in the interclump medium would be responsible for the observed dichroic polarization at IR. Specifically, the IR radiation from the clumps passes through the aligned dust grains in the interclump medium. We now define the ratio of the optical depth of the clump, $\tau^{\rm c}$, and interclump medium, $\tau^{\rm m}$, with the contrast parameter $C = \tau^{\rm c}/\tau^{\rm m}$. C is a positive quantity, with $C = 1$, describing the obscuring dusty material in a smooth distribution of dust, where large values of C will enhance the clumpy distribution of dust grains. An optical depth of the clumps of $\tau_{\rm v}^{\rm c} = 49^{+4}_{-3}$ was took from Alonso-Herrero et al. (2011) using CLUMPY models to fit the nuclear IR spectral energy distribution (SED) of NGC 1068. Based on our polarization model, the minimum visual extinction to be compatible with the observations is $A_{\rm v} = 8$ mag, or $\tau_{\rm v} = 8.7$. Taking this value as the extinction of the interclump medium, we obtain a contrast of $C = 5.6^{+0.4}_{-0.7}$ at V band. This result favours the clumpy distribution of dust versus a smooth-density obscuring material. The clumpy models (Stalevski et al. 2012; Siebenmorgen, Heymann & Efstathiou 2015) including a two-phase medium are crucial to generate SED based on the MIR polarimetric observational constraints. However, the development of these models is beyond the scope of this paper.

6 CONCLUSIONS

We presented subarcsecond resolution MIR (7.5–13 μm) imaging- and spectro-polarimetric observations of NGC 1068 obtained with CanariCam on the 10.4-m GTC. Using the wide MIR wavelength coverage, we were able to disentangle several polarized structures in the complex 3 × 2 arcsec (180 × 120 pc) central region through their polarization signatures. At all wavelengths, we found:

(i) Northern ionization cone: the most prominent feature is the uniform PA of polarization, ∼44°, with an extension of ∼1.5 × 1.0 arcsec (90 × 60 pc). Based on our polarization model, we found that the polarization arises from dust and gas emission in the ionization cone, heated by the AGN and jet, and further extinguished by aligned dust grains in the NIR bar. In this region, we found that the *north knot*, located at ∼0.4 arcsec (24 pc) from the core, is spatially coincident with the interaction of the jet and molecular cloud. The *north knot* shows a uniform PA of polarization and a slow decrease in the degree of polarization with increasing wavelength. No silicate feature is found in the polarization spectrum of the *north knot*, suggesting that the dust grains are different from those in the ISM.

(ii) Southern ionization cone: we found a polarized feature at ∼0.16 arcsec (9.6 pc) south of the core. Based on our polarization model, the *southern feature* polarization arises from an emissive polarization component passing through a larger concentration of dust than in the northern ionization cone. For this emissive component, we cannot distinguish between (1) magnetically aligned dust grains directly heated by the jet in the southern ionization cone close to the AGN, and (2) magnetically aligned dust grains in the obscuring dusty structure surrounding the central engine. The polarization spectrum shows a prominent silicate feature, suggesting that different dust grains composition or sizes may be present in the northern and southern ionization cones.

(iii) Obscuring dusty structure: an upper limit of 0.3 per cent in the degree of polarization from the core is detected in our observations. Based on our polarization model, the expected polarization from extrapolating the NIR absorptive component is $\lesssim$0.1 per cent in the 8–13 μm wavelength range. We note that while there could be a component of polarized emission from those dust grains, if they are sufficiently warm to emit in the MIR, the uncertainties in estimating any contribution are very large. We suggested that the MIR polarization arises from the passage of MIR radiation through aligned dust grains in the shielded edges of the clumps located at the innermost regions of the obscuring dusty structure (Fig. 10). Alternatively, an obscuring clumpy structure with an interclump medium, and with an optical depth contrast between the clumps and the interclump medium of $C = 5.6^{+0.4}_{-0.7}$ at V band, can also reproduce the upper limit of the degree of polarization in our observations.

The subarcsecond resolution polarization observations of NGC 1068 demonstrate that there are a number of different regions and mechanism operating within the central 10 s of parsecs in this AGN. Similar complexity may occur in other AGNs, where the current observations cannot resolve these structures. Further subarcsecond MIR imaging- and spectro-polarimetric observations to several AGNs are crucial to find ordinary and/or extraordinary

properties in AGN allowing us to refine and/or modify the AGN unified model.

ACKNOWLEDGEMENTS

It is a pleasure to acknowledge discussion with R. Mason. We would like to thank the anonymous referee for their useful comments, which improved the paper significantly. Based on observations made with the Gran Telescopio CANARIAS (GTC), installed in the Spanish Observatorio del Roque de los Muchachos of the Instituto de Astrofísica de Canarias, in the island of La Palma. ELR and CP acknowledge support from the University of Texas at San Antonio. CP acknowledges support from NSF-0904421 grant. AA-H acknowledges financial support from the Spanish Ministry of Economy and Competitiveness (MINECO) under the 2011 Severo Ochoa Program MINECO SEV-2011- 0187. AA-H acknowledges financial support from the Spanish Ministry of Economy and Competitiveness through grant AYA2012-31447, which is partly funded by the FEDER program, PE from grant AYA2012-31277, and LC from grant AYA2012-32295. RN acknowledges support by FONDECYT grant no. 3140436. CRA is supported by a Marie Curie Intra European Fellowship within the 7th European Community Framework Programme (PIEF-GA-2012-327934). EP acknowledges support from NSF grant AST-0904896.

REFERENCES

Aitken D. K., Briggs G., Bailey J. A., Roche P. F., Hough J. H., 1984, Nature, 310, 660
Aitken D. K., Briggs G. P., Roche P. F., Bailey J. A., Hough J. H., 1986, MNRAS, 218, 363
Aitken D. K., Smith C. H., Roche P. F., 1989, MNRAS, 236, 919
Aitken D. K., Hough J. H., Roche P. F., Smith C. H., Wright C. M., 2004, MNRAS, 348, 279
Alloin D., Pantin E., Lagage P. O., Granato G. L., 2000, A&A, 363, 926
Alonso-Herrero A. et al., 2011, ApJ, 736, 82
Antonucci R., 1993, ARA&A, 31, 473
Antonucci R. R. J., Miller J. S., 1985, ApJ, 297, 621
Antonucci R., Hurt T., Miller J., 1994, ApJ, 430, 210
Bailey J., Axon D. J., Hough J. H., Ward M. J., McLean I., Heathcote S. R., 1988, MNRAS, 234, 899
Bock J. J., Marsh K. A., Ressler M. E., Werner M. W., 1998, ApJ, 504, L5
Bock J. J. et al., 2000, AJ, 120, 2904
Braatz J. A., Wilson A. S., Gezari D. Y., Varosi F., Beichman C. A., 1993, ApJ, 409, L5
Bruhweiler F. C., Miskey C. L., Smith A. M., Landsman W., Malumuth E., 2001, ApJ, 546, 866
Cameron M., Storey J. W. V., Rotaciuc V., Genzel R., Verstraete L., Drapatz S., Siebenmorgen R., Lee T. J., 1993, ApJ, 419, 136
Capetti A., Axon D. J., Macchetto F., Sparks W. B., Boksenberg A., 1995, ApJ, 446, 155
Cohen M., Davies J. K., 1995, MNRAS, 276, 715
Crenshaw D. M., Kraemer S. B., 2000, ApJ, 532, 247
Das V., Crenshaw D. M., Kraemer S. B., 2007, ApJ, 656, 699
Drury L. O., 1983, Rep. Prog. Phys., 46, 973
Emsellem E., Fathi K., Wozniak H., Ferruit P., Mundell C. G., Schinnerer E., 2006, MNRAS, 365, 367
Evans I. N., Ford H. C., Kinney A. L., Antonucci R. R. J., Armus L., Caganoff S., 1991, ApJ, 369, L27
Galliano E., Pantin E., Alloin D., Lagage P. O., 2005, MNRAS, 363, L1
Gallimore J. F., Baum S. A., O'Dea C. P., 1996, ApJ, 464, 198
Gallimore J. F., Henkel C., Baum S. A., Glass I. S., Claussen M. J., Prieto M. A., Von Kap-herr A., 2001, ApJ, 556, 694
Gallimore J. F., Baum S. A., O'Dea C. P., 2004, ApJ, 613, 794
Gao J., Li A., Jiang B. W., 2013, Earth Planets Space, 65, 1127
García-Burillo S. et al., 2014, A&A, 567, A125
García-Gómez C., Athanassoula E., Barberà C., 2002, A&A, 389, 68
Greenhill L. J., Ellingsen S. P., Norris R. P., Gough R. G., Sinclair M. W., Moran J. M., Mushotzky R., 1997, ApJ, 474, L103
Hagiwara Y., Kohno K., Kawabe R., Nakai N., 1997, PASJ, 49, 171
Imanishi M., Ueno S., 2000, ApJ, 535, 626
Jaffe W. et al., 2004, Nature, 429, 47
Knacke R. F., Capps R. W., 1974, ApJ, 192, L19
Kraemer S. B., Crenshaw D. M., 2000a, ApJ, 532, 256
Kraemer S. B., Crenshaw D. M., 2000b, ApJ, 544, 763
Kraemer S. B., Sharma N., Turner T. J., George I. M., Crenshaw D. M., 2015, ApJ, 798, 53
Krist J. E., Hook R. N., Stoehr F., 2011, Proc. SPIE Conf. Ser. Vol. 8127, 81270J-1
Lawrence A., 1991, MNRAS, 252, 586
Lawrence A., Elvis M., 2010, ApJ, 714, 561
Lebofsky M. J., Kemp J. C., Rieke G. H., 1978, ApJ, 222, 95
Levenson N. A., Sirocky M. M., Hao L., Spoon H. W. W., Marshall J. A., Elitzur M., Houck J. R., 2007, ApJ, 654, L45
López-Gonzaga N., Jaffe W., Burtscher L., Tristram K. R. W., Meisenheimer K., 2014, A&A, 565, A71
Lopez-Rodriguez E., 2016, MNRAS, 455, 2656
Lopez-Rodriguez E. et al., 2015, MNRAS, 452, 1902
Lumsden S. L., Moore T. J. T., Smith C., Fujiyoshi T., Bland-Hawthorn J., Ward M. J., 1999, MNRAS, 303, 209
Macchetto F., Capetti A., Sparks W. B., Axon D. J., Boksenberg A., 1994, ApJ, 435, L15
Mason R. E., Geballe T. R., Packham C., Levenson N. A., Elitzur M., Fisher R. S., Perlman E., 2006, ApJ, 640, 612
Miyoshi M., Moran J., Herrnstein J., Greenhill L., Nakai N., Diamond P., Inoue M., 1995, Nature, 373, 127
Nenkova M., Ivezić Ž., Elitzur M., 2002, ApJ, 570, L9
Nenkova M., Sirocky M. M., Ivezić Ž., Elitzur M., 2008a, ApJ, 685, 147
Nenkova M., Sirocky M. M., Nikutta R., Ivezić Ž., Elitzur M., 2008b, ApJ, 685, 160
Neufeld D. A., Maloney P. R., Conger S., 1994, ApJ, 436, L127
Packham C., Young S., Hough J. H., Axon D. J., Bailey J. A., 1997, MNRAS, 288, 375
Packham C., Hough J. H., Telesco C. M., 2005, in Adamson A., Aspin C., Davis C., Fujiyoshi T., eds, ASP Conf. Ser. Vol. 343, Astronomical Polarimetry: Current Status and Future Directions. Astron. Soc. Pac., San Francisco, p. 38
Packham C. et al., 2007, ApJ, 661, L29
Packham C., Mason R. E., Boreman G. D., 2008, Opt. Eng., Bellingham, 47, 126401
Pier E. A., Krolik J. H., 1992, ApJ, 401, 99
Poncelet A., Doucet C., Perrin G., Sol H., Lagage P. O., 2007, A&A, 472, 823
Raban D., Jaffe W., Röttgering H., Meisenheimer K., Tristram K. R. W., 2009, MNRAS, 394, 1325
Radomski J. T. et al., 2008, ApJ, 681, 141
Roche P. F., Aitken D. K., 1984, MNRAS, 208, 481
Scarrott S. M., Rolph C. D., Wolstencroft R. W., Tadhunter C. N., 1991, MNRAS, 249, 16
Schinnerer E., Eckart A., Tacconi L. J., Genzel R., Downes D., 2000, ApJ, 533, 850
Scoville N. Z., Matthews K., Carico D. P., Sanders D. B., 1988, ApJ, 327, L61
Serkowski K., Mathewson D. S., Ford V. L., 1975, ApJ, 196, 261
Siebenmorgen R., Heymann F., Efstathiou A., 2015, AA, in press
Simpson J. P., Colgan S. W. J., Erickson E. F., Hines D. C., Schultz A. S. B., Trammell S. R., 2002, ApJ, 574, 95
Smith C. H., Wright C. M., Aitken D. K., Roche P. F., Hough J. H., 2000, MNRAS, 312, 327
Stalevski M., Fritz J., Baes M., Nakos T., Popović L. Č., 2012, MNRAS, 420, 2756
Storchi-Bergmann T., Riffel R. A., Riffel R., Diniz M. R., Borges Vale T., McGregor P. J., 2012, ApJ, 755, 87

Telesco C. M. et al., 2003, in Iye M., Moorwood A. F. M., eds, Proc. SPIE Conf. Ser. Vol. 4841, Instrument Design and Performance for Optical/Infrared Ground-based Telescopes. SPIE, Bellingham, p. 913
Thompson R. I., Chary R.-R., Corbin M. R., Epps H., 2001, ApJ, 558, L97
Tinbergen J., 2005, Astronomical Polarimetry. Cambridge Univ. Press, Cambridge
Tomono D., Doi Y., Usuda T., Nishimura T., 2001, ApJ, 557, 637
Tomono D., Terada H., Kobayashi N., 2006, ApJ, 646, 774
Trotter A. S., Greenhill L. J., Moran J. M., Reid M. J., Irwin J. A., Lo K.-Y., 1998, ApJ, 495, 740
Urry C. M., Padovani P., 1995, PASP, 107, 803
Wardle J. F. C., Kronberg P. P., 1974, ApJ, 194, 249
Watanabe M., Nagata T., Sato S., Nakaya H., Hough J. H., 2003, ApJ, 591, 714
Weingartner J. C., Draine B. T., 2001, ApJ, 548, 296
Wilson A. S., Braatz J. A., Henkel C., 1995, ApJ, 455, L127
Young S., Hough J. H., Axon D. J., Bailey J. A., Ward M. J., 1995, MNRAS, 272, 513

This paper has been typeset from a TEX/LATEX file prepared by the author.